Accepted Manuscript

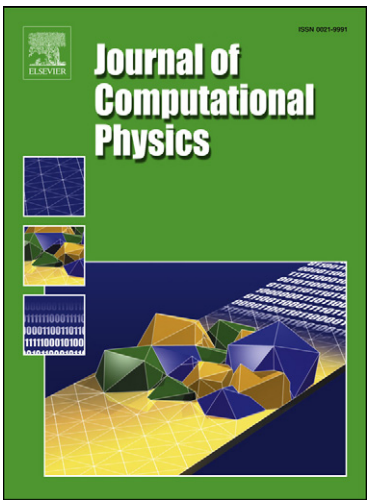

Three-dimensional control-volume distributed multi-point flux approximation coupled with a lower-dimensional surface fracture model

Raheel Ahmed, Michael G. Edwards, Sadok Lamine, Bastiaan A.H. Huisman, Mayur Pal

PII: S0021-9991(15)00660-9
DOI: http://dx.doi.org/10.1016/j.jcp.2015.10.001
Reference: YJCPH 6155

To appear in: *Journal of Computational Physics*

Received date: 1 February 2015
Revised date: 16 September 2015
Accepted date: 1 October 2015

Please cite this article in press as: R. Ahmed et al., Three-dimensional control-volume distributed multi-point flux approximation coupled with a lower-dimensional surface fracture model, *J. Comput. Phys.* (2015), http://dx.doi.org/10.1016/j.jcp.2015.10.001

Three-dimensional control-volume distributed multi-point flux approximation coupled with a lower-dimensional surface fracture model

Raheel Ahmed[a,*], Michael G. Edwards[a], Sadok Lamine[b], Bastiaan A.H. Huisman[b], Mayur Pal[c]

[a] *ZCCE, College of Engineering, Swansea University, Swansea SA2 8PP, Wales UK*
[b] *Shell Global Solutions International B.V., Kessler Park 1, 2288 GS, Rijswijk, The Netherlands.*
[c] *Maersk Oil and Gas A/S, 1263 Copenhagen, Denmark.*

Abstract

A novel cell-centred control-volume distributed multi-point flux approximation (CVD-MPFA) finite-volume formulation is presented for discrete fracture-matrix simulations on unstructured grids in three-dimensions (3D). The grid is aligned with fractures and barriers which are then modelled as lower-dimensional surface interfaces located between the matrix cells in the physical domain. The three-dimensional pressure equation is solved in the matrix domain coupled with a two-dimensional (2D) surface pressure equation solved over fracture networks via a novel surface CVD-MPFA formulation. The CVD-MPFA formulation naturally handles fractures with anisotropic permeabilities on unstructured grids. Matrix-fracture fluxes are expressed in terms of matrix and fracture pressures and define the transfer function, which is added to the lower-dimensional flow equation and couples the three-dimensional and surface systems. An additional transmission condition is used between matrix cells adjacent to low permeable fractures to couple the velocity and pressure jump across the fractures. Convergence and accuracy of the lower-dimensional fracture model is assessed for highly anisotropic fractures having a range of apertures and permeability tensors. A transport equation for tracer flow is coupled via the Darcy flux for single and intersecting fractures. The lower-dimensional approximation for intersecting fractures avoids the more restrictive CFL condition corresponding to the equi-dimensional approximation with explicit time discretisation. Lower-dimensional fracture model results are compared with equi-dimensional model results. Fractures and barriers are efficiently modelled by lower-dimensional interfaces which yield comparable results to those of the equi-dimensional model. Pressure continuity is built into the model across highly conductive fractures, leading to reduced local degrees of freedom in the CVD-MPFA approximation. The formulation is applied to geologically complex fracture networks in three-dimensions. The effects of the fracture permeability, aperture and grid resolution are also assessed with respect to convergence and computational cost.

Keywords: Three-dimensions, CVD-MPFA, fracture network, lower-dimensional, interfaces, fracture matrix transfer

*Corresponding author
Email addresses: R.AHMED.642142@swansea.ac.uk (Raheel Ahmed), m.g.edwards@swansea.ac.uk (Michael G. Edwards)

1. Introduction

Understanding of fluid flow through a fractured porous medium has immense importance in energy production and environmental problems. The oil industry has a special interest because an estimated 60% of the world's remaining oil reserves reside in fractured formations [1]. In addition to oil and gas production fracture modelling is of interest in determining carbon sequestration strategies, radioactive waste management in the subsurface [2], and flow of non-aqueous-phase liquids in aquifers. Fractures are a system of rock discontinuities e.g. faults, joints and fissures, that occur in porous media with apertures having widths ranging over scales from microns to centimetres [3]. Open fractures act as preferential fluid flow paths above a certain aperture and size whereas cemented fractures can act as flow barriers. Flow, in any rock, is affected by a few large fractures, by a dense network of small fractures, or by a combination of fractures of varying length scales ranging from microns to hundreds of kilometres [4, 5]. Usually the matrix provides the storage for the fluid while fractures provide the main fluid flow paths. For example in two-phase flow, fractures may form the predominant flow paths for a particular phase and the less permeable matrix may become the flow region for the other phase [6].

Because of the importance of fractures in the reservoirs, increasing effort is being devoted to development of efficient and accurate numerical methods to simulate the fluid flow through fractured porous media. Dual-porosity/permeability models, developed in [7, 8, 9], have traditionally been used for the last few decades. Flow transfer terms are defined between the fracture and matrix systems. These transfer terms depend on the *shape factor*, average pressure difference between two domains and further physical parameters in the case of multi-phase flow [10]. The shape factor is not straightforward to determine and is not available in the presence of capillarity and gravity for two-phase flow [2]. Also, barriers cannot be modelled by dual-porosity/permeability models. Moreover, these models are based on the assumption that fracture systems are dense so inaccurate results are given for large scale fractures. As a result, the discrete-fracture model(DFM) was developed; see e.g. [11, 12, 13, 14, 15, 16], which is attractive for large scale and sparse fracture systems. In this model actual geometry and location of the fracture are honoured in the domain. Unlike the dual-porosity model; the effect of individual fractures on fluid flow can be determined and fluid transfer between the fracture and matrix is more straightforward and consistent. Generally, fractures are modelled by (n-1) dimensional elements in an n-dimensional domain e.g. in two-dimensions (2D), fractures are represented by lines at the edges of the polygonal matrix elements while in three-dimensions (3D) fracture systems are modelled as polygonal surfaces between the polyhedral matrix elements. Equi-dimensional representation of fractures [17], are not popular because of complexity and computational cost contributed by thin cells. In the equi-dimensional model, the control-volume at the intersection of the fractures is of the dimensions of fracture aperture which reduces the time-step size in the numerical model [2]. Also, in our experience with this method we have observed that a small control-volume increases the condition number of the global linear system which increases the computational cost for the solution of the system, consistent with [18].

In the discrete-fracture method, rock-matrix and fracture elements coincide at the interface, so an unstructured grid is used to honour the explicit fracture geometry (see [19, 20]). Also, the matrix cells near the fracture are small enough to conform to the complex fracture-network geometry. Small cells lead to a large numerical system to be solved. Because of grid conformity, application of this model to dynamic fracture networks requires a dynamic grid generator with a conforming mesh where the grid is updated because of generation of new fractures [21, p. 72]. The discrete-fracture model would be increasingly costly for small scale fractures and any cases with large numbers of fractures, which would lead to locally dense unstructured grids in-turn leading to high computational cost. Hierarchical fracture models have been presented in [22, 23] for two-dimensional flow simulation in a fractured porous medium. In this approach, small scale fractures are homogenized into the matrix medium and their effects are added to the matrix permeability. Large scale fractures are explicitly modelled as major fluid conduits embedded into a non-conforming structured mesh. Other techniques based on discontinuity finite element modelling and extended-finite element method (XFEM) for embedded fractures into non-conforming mesh are presented in [24, 25, 26]. Recently, a continuum voxel approach has been presented in [27] where hydraulic properties of a fracture network are mapped onto a stair-like regular mesh to avoid the intense meshing issue for discrete-fractures. A technique of multi-scale philosophy is presented in [28] to reduce the number of degrees of freedom for the fracture-only simulations. Various numerical methods have been used with DFM for single and multiphase flow in fractured porous media. Mass conservative methods include control-volume finite-element (CVFE) [6, 29], cell-centred finite-volume (CCFV) [30, 18], mixed finite-element (MFE) [16, 2, 31] and recently developed vertex-approximate-gradient (VAG) scheme [32] and mimetic finite-difference method [33]. CVFE is not control volume distributed and is not flux-continuous for heterogeneous porous medium. MFE is locally flux-continuous and consistent but is computationally expensive because of higher degrees of freedom per cell as compared to CCFV and CVFE.

Herein, we will focus on a locally conservative cell-centred finite-volume (CCFV) formulation coupled with discrete-fracture networks, in particular we use the control-volume distributed multi-point flux approximation (CVD-MPFA) [34, 35]. We choose CVD-MPFA because the method is flux-continuous and consistent for unstructured grids and heterogeneous porous media and uses a single degree of freedom per control-volume (grid cell in this case). Note that commercial simulators also use a single degree of freedom per grid cell. We use a conforming unstructured mesh to capture the heterogeneity of a porous medium with fractures. Recently, Sandve et al. [18] used the CVD-MPFA O-method (TPS with default quadrature $q = 1$), for two-dimensional discrete-fracture and matrix simulation based on a hybrid-grid approach [30]. In the hybrid-grid approach, fractures are (n-1)D in the physical mesh and are expanded to nD in the computational domain. The nD pressure equation is solved by the usual CVD-MPFA formulation in both matrix and fractures in the computational domain. The main difference between the equi-dimensional model and hybrid-grid model is the treatment of the intermediate cell between the intersecting fractures. In a hybrid-grid, the intermediate cell is assumed to be of small size so that pressure variation is zero in that cell to avoid the complexity that

would be incurred by the small size of intermediate cell in the equi-dimensional model.

In this work, we present a 3D CVD-MPFA formulation applied to a 3D matrix coupled with a 2D fracture model. The matrix is defined over a 3D unstructured mesh, and fractures are defined by 2D surface meshes. A novel surface CVD-MPFA method is introduced to approximate the 2D surface pressure equation describing flow in the fractures. In this formulation, the 3D pressure equation is solved in the matrix domain with coupling for surface fracture networks where the 2D surface pressure equation is solved. This work represents a 3D extension of the 2D CVD-MPFA formulation coupled with a 1D fracture model presented in [36, 37]. In this paper we refer to the 3D matrix coupled with a 2D fracture model as a lower-dimensional fracture model (2D surface fracture model in 3D context) because fractures are strictly lower-dimensional. The coupled CVD-MPFA formulation can easily be incorporated into current CVD-MPFA based simulators. Moreover, we compare the pressure and tracer transport fields computed by the lower-dimensional fracture model with the results of an explicit equi-dimensional model on unstructured meshes. The lower-dimensional fracture model gives comparable results to those given by the equi-dimensional model for domains involving fractures and barriers. Highly conductive fractures can be modelled by the lower-dimensional model, with continuous pressure approximation across fractures, without adding extra degrees of freedom locally for the cluster of cells as required by the hybrid-grid method. An additional transmission condition is used between matrix cells adjacent to low permeable fractures to couple the velocity and pressure jump across the fractures.

The outline of the paper is as follows; we present the flow equations in section 2. We present our CVD-MPFA formulation in section 3 for the 3D matrix coupled with 2D surface fractures. The transport model for the lower-dimensional fractures is discussed in section 4. Numerical tests are presented in section 5 to compare the lower-dimensional and equi-dimensional fracture models. We draw our conclusions based on numerical tests in the last section 6.

2. Flow equations

We focus on the discretisation of an elliptic partial differential equation for pressure by a CVD-MPFA method for DFM. The pressure equation arises from Darcy's law and mass conservation for single phase flow (a similar method is also applicable to multiphase flow). The resulting elliptic pressure equation

$$-\nabla \cdot \frac{\boldsymbol{k}}{\mu} \nabla \phi = q_c \tag{1}$$

is solved on a domain Ω, where ϕ is the pressure and q_c is any known source term, $\boldsymbol{k}$ is the permeability tensor and μ is the viscosity of the fluid. As usual in single phase flow we let $\boldsymbol{K} = \frac{\boldsymbol{k}}{\mu}$ denote the (abbreviated) possibly heterogeneous spatially varying, symmetric permeability tensor of second rank with possibly non-zero off-diagonal coefficients written, in general, as; $\boldsymbol{K} = \begin{pmatrix} K_{11} & K_{12} & K_{13} \\ K_{12} & K_{22} & K_{23} \\ K_{13} & K_{23} & K_{33} \end{pmatrix}$. The Darcy velocity is given by $\boldsymbol{v} = -\boldsymbol{K}\nabla\phi$. Eq. (1) is solved here subject to Dirichlet and/or Neumann boundary conditions which are

$\phi = h(\boldsymbol{x})$ and $(\boldsymbol{K}\nabla\phi)\cdot\boldsymbol{n} = g(\boldsymbol{x})$ respectively on the domain boundary $\delta\Omega$, where h and g are scalar fields defined at the boundary and $\boldsymbol{n}$ is the outward normal vector at the boundary. Pressure and/or flow rate may also be prescribed at wells in the domain. While this CVD-MPFA formulation is consistent and applicable to problems with full permeability tensors in both the rock matrix and fracture, the test cases presented involve fractures with diagonal tensors, where the fracture tensor is of the form $\boldsymbol{K_f} = \begin{pmatrix} K_{ft_1} & 0.0 & 0.0 \\ 0.0 & K_{ft_2} & 0.0 \\ 0.0 & 0.0 & K_{fn} \end{pmatrix}$. Usually, $K_{ft_1}, K_{ft_2} \leq a_h^2/12$ which is the maximum tangential permeability of the region, of width a_h, when flow is between two parallel plates without tortuosity or cementation.

The mass conservation equation for tracer transport ignoring dispersion is written as the advection equation below:

$$\varphi\frac{\partial c}{\partial t} + \nabla\cdot(\boldsymbol{v}c) = q_c \tag{2}$$

where, c is the tracer concentration and φ is the porosity which can be taken as unity here for simplicity.

3. CVD-MPFA formulation with coupling for fractures

Here, we will investigate a lower-dimensional fracture model where the 2D pressure equation is solved over fracture surfaces, coupled with the 3D pressure equation in the matrix. We incorporate the lower-dimensional fracture model for fractures and barriers, presented by V. Martin et al. [16] in context of 2D MFE, into the 3D CVD-MPFA framework. F. Heße et al. [38] has summarized the assessment of lower-dimensional modelling of fractures and concluded that such modelling is applicable "when the matrix-diffusion coefficient is small or like in field experiments, the sub-surface parameters are determined with little accuracy". Highly conductive fractures can be treated as lower-dimensional cells without including extra matrix-fracture interfaces thus reducing the local degrees of freedom of a cluster when compared to the hybrid-grid method. Many authors e.g. [39, 2, 23], have efficiently treated lower-dimensional fracture cells with various numerical methods for the solution of elliptic pressure equation. Here, we focus on the CVD-MPFA method for fractured media because the method is locally flux-continuous, consistent, applicable on unstructured grids and has a single degree of freedom globally per grid-cell. There are two variations of lower-dimensional fracture model (i) continuous pressure model where pressure across the fracture is assumed continuous and (ii) discontinuous pressure model where discontinuity in pressure is allowed across the fracture for matrix-fracture flux computation which is more generic to model fractures and barriers alike. Moreover, we use the transfer function approach, presented by Hoteit et al. [2], to couple matrix and fracture domains. For the matrix domain the 3D equation is solved while the 2D equation is solved over fracture cells:

$$-\nabla\cdot\boldsymbol{K}_m\nabla\phi = q_{cm} \quad \text{in} \quad \Omega_m \tag{3}$$

$$-\nabla_t\cdot\boldsymbol{K}_{f,t}\nabla_t\phi_f + q_f = q_{cf} \quad \text{in} \quad \Omega_f \tag{4}$$

where, ∇_t and $\boldsymbol{K}_{f,t}$ are the respective longitudinal (surface tangent) gradient operator and permeability of fracture. q_{cm} and q_{cf} are known source terms for the rock matrix and fracture respectively. Transfer function, q_f, accounts for the net normal flux transfer between matrix and fracture cells, resulting from the dimensionality reduction to obtain (n-1)D equation (4). Matrix-fracture flux is also added naturally in the formulation for the matrix cells discussed later on. The flow equations (3) and (4) are integrated over the grid cell control volumes using the Gauss divergence theorem to obtain,

$$-\oint_{\delta\Omega_{m\,i}} (\boldsymbol{K}_m \nabla\phi)\cdot\boldsymbol{n}_i dS = \bar{q}_{cm} \tag{5}$$

$$-\oint_{\delta\Omega_{f_j}} (\boldsymbol{K}_{f,t}\nabla_t\phi_f)\cdot\boldsymbol{n}_j dS + Q_f = \bar{q}_{cf} \tag{6}$$

where $\bar{q}_{cm} = \int_{\Omega_{m\,i}} q_{cm}\, dV$; any known source term for matrix cell $\Omega_{m\,i}$. $\bar{q}_{cf} = \int_{\Omega_{f_j}} q_{cf}\, dV$; known source term for fracture cell Ω_{f_j}. Moreover, $Q_f = \int_{\Omega_{f_j}} q_f\, dV$, transfer function for the lower-dimensional fracture cell Ω_{f_j}.

3.1. Matrix-matrix and matrix-fracture fluxes

For the cell-centred finite-volume method, control-volumes are defined by the grid cells which can be the tetrahedrons, hexahedrons, prisms or any polyhedral shapes in three-dimensions (3D). The primal grid nodes form corner points of the primal grid cells and are called vertices. The numerical solution is associated with the grid point, which is usually the cell centroid, as in this work. Flow variables and physical properties are assigned to the grid cells i.e. control-volume distributed (CVD). Continuous flux and pressure constraints are imposed locally with respect to each *cluster* of cells that are attached to a common grid vertex. A *dual-cell* is introduced which is defined by connecting each grid point with centres of the respective cell faces and edges that are attached to the cluster vertex. The resulting polyhedron around a cluster vertex is called a dual-cell. A cluster and the dual-cell for 8 tetrahedrons are depicted in Fig. 1a. *Sub-cell* hexahedrons are formed when dual-cells overlay the primal cells. Each sub-cell is defined by joining the grid point to the centres of the faces connected to the cluster vertex and by joining the face centres to the midpoints of corresponding edges. The number of the sub-cells in a grid cell are the same as the number of the vertices defining the grid cell; four for tetrahedron, six for prism, five for pyramid and eight for a hexahedron. A tetrahedron decomposed into four sub-cells is depicted in Fig. 1b. A sub-interface is the name of the quadrilateral that is formed when a sub-cell intersects the face of the grid cell. The (quadrilateral) sub-interface is constructed by connecting the face centre to the mid-points of the edges then to the cluster vertex. There are three sub-interfaces for a sub-cell connected to the cluster vertex. In the CVD-MPFA method, normal flux continuity and pressure continuity are fulfilled for every sub-interface of the cluster. In this work, we employ the tetrahedron pressure support (TPS) formulation [35]. An auxiliary interface pressure is introduced on each sub-interface to ensure point-wise pressure continuity. The continuity point is defined by the parametric variation in $[0 < q \leq 1]$ along the diagonal of the sub-interface, where $q = 0$ corresponds to the cluster vertex (which is avoided) and

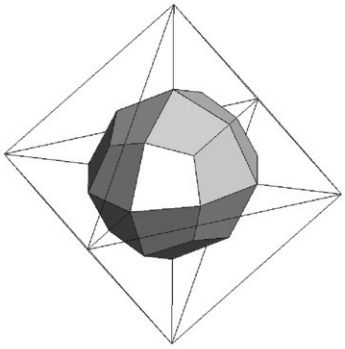

(a) Cluster and the dual of the tetrahedral matrix cells.

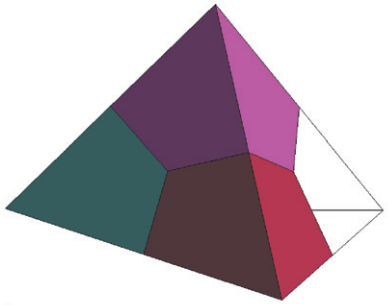

(b) Sub-cells of a tetrahedron cell

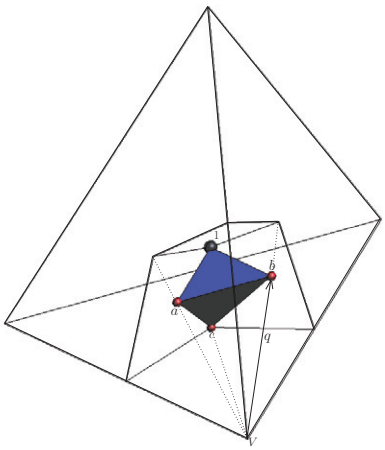

(c) Tetrahedral pressure support for a sub-cell

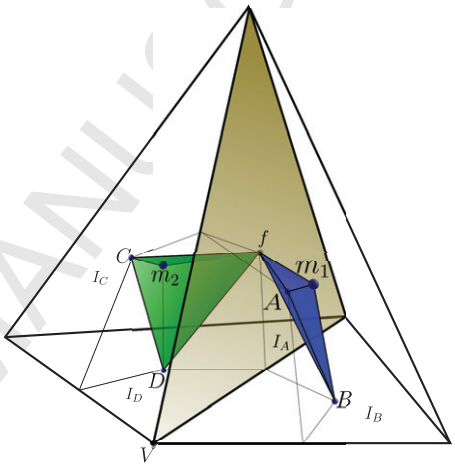

(d) Two neighbouring tetrahedrons. Sub-cells and sub-interface are depicted, attached to the cluster vertex V. TPS for the cells are also shown (in green and blue) for $q = 1$.

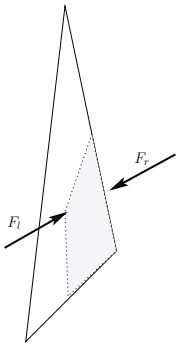

(e) Discontinuous fluxes across the interface which is fracture cell

Figure 1: CVD-MPFA framework in 3D

$q = 1$ corresponds to a face centre and is the standard default point. Double parameters (q_1, q_2) can also be used to define continuity points on sub-interfaces, cf. [40, 35]. In this scheme, pressure is assumed piecewise linear in a tetrahedron region defined by joining the grid point with the auxiliary continuity points on three

faces connected to the cluster vertex. Pressure in the tetrahedral region of the cell 1, as shown in Fig. 1c, is written in terms of the barycentric coordinate referential (ξ, η, γ) as $\phi = (1-\xi-\eta-\gamma)\phi_1 + \xi\phi_a + \eta\phi_b + \gamma\phi_c$. A piecewise constant pressure gradient vector can be formed over each sub-cell from the tetrahedral linear pressure field from which the Darcy velocity vector is determined in each sub-cell. The Darcy velocity is resolved along the outward normals to three sub-interfaces of the sub-cell. So, the normal flux at a sub-interface is written as,

$$F = \boldsymbol{v_h} \cdot \boldsymbol{dA_h} = -(T_{11}\phi_\xi + T_{12}\phi_\eta + T_{13}\phi_\gamma) \tag{7}$$

where, $\boldsymbol{T} = \boldsymbol{T}(q)$ is an approximation of the general Piola tensor and define the coefficients of $(\phi_\xi, \phi_\eta, \phi_\gamma)$. For the full definition of general tensor we refer to [35]. Similarly, fluxes are determined on both sides of the sub-interfaces in a cluster. Continuity of flux is imposed on all the sub-interfaces, between matrix cells, (but not fracture cells) to eliminate the pressure associated with matrix sub-interfaces. Next, we present the flux formulation in the case of the fracture cell between the matrix cells.

3.1.1. Continuous pressure model

For high permeability and low aperture, the jump in pressure across the fracture is very low. Pressure can be assumed constant across the width of fracture but the velocity jump is not zero. In this case, point-wise pressure continuity is imposed on the 2D fracture sub-interfaces, between matrix cells. Consider an interface, between two matrix cells, which is a lower-dimensional (2D) fracture cell, as shown in Fig. 1d. Outward flux on sub-interface I_f from sub-cell of cell m_1 can be written as,

$$F^1_{I_f} = -(T^1_{11}\phi_\xi + T^1_{12}\phi_\eta + T^1_{13}\phi_\gamma)|^1_{I_f} \tag{8}$$

where, $\begin{pmatrix} \phi_\xi \\ \phi_\eta \\ \phi_\gamma \end{pmatrix} = \begin{pmatrix} \phi_f - \phi_{m_1} \\ \phi_A - \phi_{m_1} \\ \phi_B - \phi_{m_1} \end{pmatrix}$

Similarly, from sub-cell of cell m_2, the outward flux on sub-interface I_f can be written as,

$$F^2_{I_f} = -(T^2_{21}\phi_\xi + T^2_{22}\phi_\eta + T^2_{23}\phi_\gamma)|^2_{I_f} \tag{9}$$

where, $\begin{pmatrix} \phi_\xi \\ \phi_\eta \\ \phi_\gamma \end{pmatrix} = \begin{pmatrix} \phi_C - \phi_{m_2} \\ \phi_f - \phi_{m_2} \\ \phi_D - \phi_{m_2} \end{pmatrix}$

Fluxes defined by Eq. (8) and Eq. (9) are discontinuous across a 2D surface fracture cell f, but the pressure of fracture cell ϕ_f is continuous and is unknown. The fluxes on the n_{fl} sub-interfaces of the cluster can be formulated in the combined simple form of matrices as follows:

$$\boldsymbol{F} = A^{n_{fl}\times n_m}\Phi_m + B^{n_{fl}\times n_i}\Phi_i + C^{n_{fl}\times n_f}\Phi_f \tag{10}$$

where, Φ_m is the vector of pressures associated with the centres of the n_m matrix cells in the cluster, Φ_i is the vector of pressures associated with the n_i sub-interfaces, between matrix cells (without fractures), and Φ_f is the vector of pressures associated with the n_f interfaces, which are 2D fracture cells in the cluster. As usual, pressures associated with the sub-interfaces which are not fracture cells, are eliminated by imposing continuity of fluxes across these sub-interfaces.

$$A_L^{n_i \times n_m}\Phi_m + B_L^{n_i \times n_i}\Phi_i + C_L^{n_i \times n_f}\Phi_f = A_R^{n_i \times n_m}\Phi_m + B_R^{n_i \times n_i}\Phi_i + C_R^{n_i \times n_f}\Phi_f \tag{11}$$

which yields,

$$\Phi_i = (B_L^{n_i \times n_i} - B_R^{n_i \times n_i})^{-1}(A_R^{n_i \times n_m} - A_L^{n_i \times n_m})\Phi_m + (B_L^{n_i \times n_i} - B_R^{n_i \times n_i})^{-1}(C_R^{n_i \times n_f} - C_L^{n_i \times n_f})\Phi_f \tag{12}$$

Fluxes are then expressed in terms of unknowns Φ_m and Φ_f only and are of the form as;

$$\boldsymbol{F} = \bar{A}^{n_{fl} \times n_m}\Phi_m + \bar{C}^{n_{fl} \times n_f}\Phi_f \tag{13}$$

where, $\bar{A}^{n_{fl} \times n_m} = A^{n_{fl} \times n_m} + B^{n_{fl} \times n_i}(B_L^{n_i \times n_i} - B_R^{n_i \times n_i})^{-1}(A_R^{n_i \times n_m} - A_L^{n_i \times n_m})$ and $\bar{C}^{n_{fl} \times n_f} = C^{n_{fl} \times n_f} + B^{n_{fl} \times n_i}(B_L^{n_i \times n_i} - B_R^{n_i \times n_i})^{-1}(C_R^{n_i \times n_f} - C_L^{n_i \times n_f})$.

3.1.2. Discontinuous pressure model

In this approximation pressure is discontinuous across the fracture sub-interfaces in the cluster. We allow pressure to vary across the fracture. The outward flux on sub-interface I_f from sub-cell of cell m_1 is written as (8) with: $\begin{pmatrix}\phi_\xi\\ \phi_\eta\\ \phi_\gamma\end{pmatrix} = \begin{pmatrix}\phi_f^- - \phi_{m_1}\\ \phi_A - \phi_{m_1}\\ \phi_B - \phi_{m_1}\end{pmatrix}$

Similarly, from sub-cell of cell m_2, the outward flux on sub-interface I_f can be written as (9) with:

$\begin{pmatrix}\phi_\xi\\ \phi_\eta\\ \phi_\gamma\end{pmatrix} = \begin{pmatrix}\phi_C - \phi_{m_2}\\ \phi_f^+ - \phi_{m_2}\\ \phi_D - \phi_{m_2}\end{pmatrix}$

The pressures ϕ_f^- and ϕ_f^+ are discontinuous across sub-interfaces of a fracture cell f in the mesh. The required n_{fl} fluxes on sub-interfaces of the cluster are formulated in the combined simple form of matrices as follows:

$$\boldsymbol{F} = A^{n_{fl} \times n_m}\Phi_m + B^{n_{fl} \times n_{if}}\Phi_{if} \tag{14}$$

where, Φ_{if} is the vector of pressures associated with the n_i sub-interfaces, between matrix cells, that are not fracture cells and $2n_f$ discontinuous pressures (ϕ_f^- and ϕ_f^+) across n_f fracture sub-interfaces. Here, $n_{if} = n_i + 2n_f$. Matrix interface pressures are eliminated via flux continuity. We use two transmission conditions (Robin type conditions) following [16] for each of the fracture sub-interfaces to eliminate discontinuous

pressures. For the sub-interface I_f, the two transmission conditions can be written as;

$$-\zeta F^1_{I_f} + \alpha_f \phi^-_f = -(1-\zeta)F^2_{I_f} + \alpha_f \phi_f \quad (15)$$

$$-\zeta F^2_{I_f} + \alpha_f \phi^+_f = -(1-\zeta)F^1_{I_f} + \alpha_f \phi_f \quad (16)$$

where, ϕ_f is the unknown pressure associated with the involved fracture cell f and specified at the centroid. $\alpha_f = \frac{2K_{f,n}}{a}$ where $K_{f,n}$ and a are the normal permeability and aperture of fracture cell. ζ is a positive parameter such that $\zeta \in]1/2, 1]$ [16]. $\zeta = 3/4$ corresponds to the second order pressure approximation across the fracture and $\zeta = 1$ corresponds to simple finite volume scheme. Discontinuous pressure across the fracture is important whenever normal permeability $K_{f,n}$ is lower than the matrix permeability and the fracture acts as a barrier. For high permeability, $\frac{1}{\alpha_f} \approx 0$ and the transmission conditions approach continuity of pressure i.e. $\phi^-_f \approx \phi^+_f \approx \phi_f$. Flux continuity conditions and transmission conditions can be written in the combined form as follows;

$$A_L^{n_{if}\times n_m}\Phi_m + B_L^{n_{if}\times n_{if}}\Phi_{if} = A_R^{n_{if}\times n_m}\Phi_m + B_R^{n_{if}\times n_{if}}\Phi_{if} + C_R^{n_{if}\times n_f}\Phi_f \quad (17)$$

rearranging,

$$\Phi_{if} = (B_L^{n_{if}\times n_{if}} - B_R^{n_{if}\times n_{if}})^{-1}(A_R^{n_{if}\times n_m} - A_L^{n_{if}\times n_m})\Phi_m + (B_L^{n_{if}\times n_{if}} - B_R^{n_{if}\times n_{if}})^{-1} C_R^{n_{if}\times n_f}\Phi_f \quad (18)$$

where C_R is diagonal with non-zeros corresponding to Eqs. (15), (16) and zero-rows corresponding to the matrix flux continuity conditions without fractures. Fluxes are expressed in terms of unknowns Φ_m and Φ_f only and are of similar form to (13). Note that, a larger local system has to be solved in (17) because of the discontinuity of fracture pressures as compared to (11) for the continuous pressure model.

Matrix-fracture transfer

Fluxes on the sub-interfaces of fractures, are retained as discontinuous for both the fracture models discussed above. The sum of the negative of the discontinuous fluxes on both sides of each fracture-interface are the transfer functions for the sub-cell of the corresponding 2D fracture cells. At interface I_f, the sum of the negative of the discontinuous fluxes is defined as the transfer function for a sub-cell of the triangular fracture cell f where:

$$Q_{f,1/3} = -F^1_{I_f} - F^2_{I_f} \quad (19)$$

In the same way we can determine the transfer functions of sub-cells of other fracture cells (as interfaces) involved in the cluster. As the fluxes have already been determined in terms of Φ_m and Φ_f in equation (13) (with an analogous equation resulting from the discontinuous pressure model), so we can write the system

of transfer functions for the corresponding fracture cells in terms of Φ_m and Φ_f as follows;

$$\boldsymbol{Q}_{f,1/3} = -\boldsymbol{F}_L - \boldsymbol{F}_R \tag{20}$$

and

$$\boldsymbol{Q}_{f,1/3} = \bar{D}^{n_f \times n_m} \Phi_m + \bar{E}^{n_f \times n_f} \Phi_f \tag{21}$$

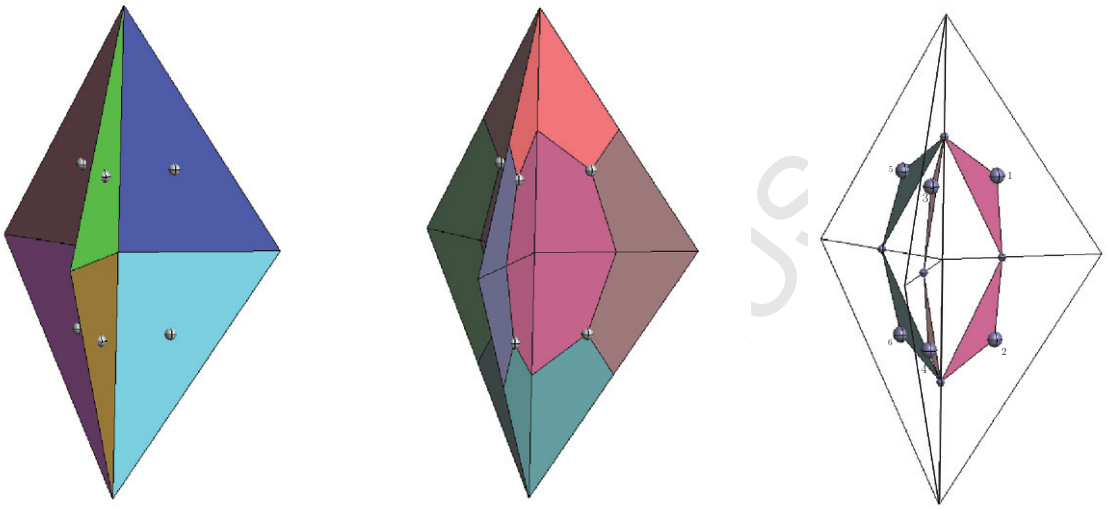

(a) Cluster of six 2D fracture cells in 3D space

(b) Sub-cells of the fracture cells

(c) TPS for the fracture cells are shown . Cell pressures are depicted by numbered balls and the auxiliary interface pressures by the smaller balls.

Figure 2: CVD-MPFA framework for 2D fracture-fracture fluxes in 3D space

3.2. Surface fracture-fracture fluxes

In this section, we present a 2D CVD-MPFA formulation for computing flow in the fractures which are surfaces in 3D space. Pressure is approximated at the centroids of the fracture cells. A cluster of six fracture cells, connected to the common vertex, is shown in Fig. 2a which form part of the discretised three intersecting fracture surfaces. The *sub-cells* are defined by joining the centroids of the fracture cells with the mid-points of the edges. The *dual-cell*, for a certain cluster, consists of the sub-cells which are common to the cluster vertex. The sub-cells are depicted in Fig. 2b where the dual-cell is illustrated around a cluster vertex, consisting of all the 2D fracture sub-cells in 3D space. We approximate the fracture-fracture fluxes for all sub-cells in terms of pressures at the fracture cell centroids and then assemble a discrete divergence equation. Pressure and flux continuity conditions are imposed on the sub-interfaces which are half of the edges (sub-interfaces) between the cells. Auxiliary interface pressures are introduced on each sub-interface to ensure point-wise pressure continuity. The continuity point is defined by the parametric variation in $[0 < q \leq 1]$ along the sub-interface where $q = 0$ corresponds to the cluster vertex (which is avoided) and $q = 1$ corresponds

to the edge mid-point and is the standard default point. Here, the symmetric positive definite (SPD) scheme of [34] with $q = 2/3$ is used for the triangular fracture cells. For each sub-cell, pressure is assumed to have a piece-wise linear variation in the triangular region defined by joining the cell centroid with the continuity points on the corresponding sub-interfaces. Referring to Fig. 2c for illustration, pressure for a sub-cell of cell 1 is written in terms of the barycentric coordinates (ξ, η) as $\phi_f = (1-\xi-\eta)\phi_1 + \xi\phi_a + \eta\phi_b$. A piecewise constant pressure gradient vector is then formed in 3D over each surface sub-cell from the piecewise linear triangular pressure field, from which the 3D Darcy velocity vector is determined in each sub-cell using the 3D projected surface gradient, written as;

$$\boldsymbol{v_h} = -\boldsymbol{K_{f,t}} \nabla_t \phi_f = -\boldsymbol{K_{f,t}} \boldsymbol{J} (\boldsymbol{J}^{tr} \boldsymbol{J})^{-1} \begin{pmatrix} \phi_\xi \\ \phi_\eta \end{pmatrix} \tag{22}$$

where, non-square Jacobian $\boldsymbol{J} = \begin{pmatrix} x_\xi & x_\eta \\ y_\xi & y_\eta \\ z_\xi & z_\eta \end{pmatrix}$ and $\boldsymbol{J}^{tr}$ is the transpose of the Jacobian $\boldsymbol{J}$, and the position vector $\boldsymbol{r}(x, y, z)$ is also expressed in terms of (ξ, η) as $\boldsymbol{r}(x, y, z) = (1-\xi-\eta)\boldsymbol{r}_1 + \xi\boldsymbol{r}_a + \eta\boldsymbol{r}_b$.

The Darcy velocity is resolved along the outward normals (scaled by value of aperture a) to two sub-interfaces of each sub-cell and the normal flux at the sub-interface is written as;

$$\mathcal{F} = (a\boldsymbol{n}) \cdot \boldsymbol{v_h} = -(T_{11}\phi_\xi + T_{12}\phi_\eta) \tag{23}$$

where, $\boldsymbol{T} = \boldsymbol{T}(q)$ defines the coefficients of (ϕ_ξ, ϕ_η). Fluxes are determined on all sub-interfaces (edges) for all sub-cells of fracture cells. All n_{fl} fluxes are expressed in the combined form;

$$\boldsymbol{\mathcal{F}} = D^{n_{fl} \times n_f} \Phi_f + E^{n_{fl} \times n_e} \Phi_e \tag{24}$$

where, $D^{n_{fl} \times n_f}$ and $E^{n_{fl} \times n_e}$ are the coefficient matrices. Φ_f and Φ_e are the vectors of pressures on cell centroids and sub-interfaces respectively. There are $n_f = 6$ pressures associated with the centroids of fracture cells, $n_e = 5$ sub-interface pressures and $n_{fl} = 12$ fluxes for the cluster shown in Fig. 2c. To eliminate the sub-interface pressures we impose mass conservation (zero divergence) on all the sub-interfaces (edges).

$$D_e^{n_e \times n_f} \Phi_f + E_e^{n_e \times n_e} \Phi_e = O \tag{25}$$

Using (25), we eliminate Φ_e in (24) and fluxes are then expressed in terms of the cell pressures only:

$$\boldsymbol{\mathcal{F}} = (D^{n_{fl} \times n_f} - E^{n_{fl} \times n_e} (E_e^{n_e \times n_e})^{-1} D_e^{n_e \times n_f}) \Phi_f \tag{26}$$

Note that, the above fracture-fracture CVD-MPFA formulation can be easily generalized to a cluster with any number of fracture cells in any orientation in 3D space. For sub-interfaces which are common to only two fracture cells, the mass conservation condition is analogous to flux continuity as in the standard CVD-MPFA

formulation.

3.3. Global linear system

The fluxes defined by (13) and (26), and transfer function defined by (21), complete the discrete finite-volume approximation of the divergence equation for every matrix cell and fracture cell. Discrete approximation of the divergence equation (5) for the matrix cell is written as;

$$\sum_{j=1}^{N_i}\sum_{k=1}^{ns_j} F_{j,k} = \bar{q}_{cm} \quad \text{for every matrix cell} \tag{27}$$

where, $F_{j,k}$ is the flux on sub-face k of the face j of the matrix cell which has N_i faces and n_{sj} is the number of sub-faces of the face j and $\bar{q}_{cm}$ is a known source term. A tetrahedral matrix cell has four faces so there are 12 outward normal fluxes on corresponding sub-faces of the cell. For those matrix cells which are in the cluster having fracture cells, fluxes are also dependent on the fracture pressure unknowns, as defined in (13). The system of equations for discrete conservation of fluxes for all the matrix cells, using (13) and (27), can be written in system form as follows;

$$G_{mm}\Phi_m + \mathcal{G}_{mf}\Phi_f = \bar{\boldsymbol{q}}_{cm} \tag{28}$$

where Φ_m is the unknown global pressure vector of all matrix cell pressures, Φ_f is the unknown global pressure vector of fracture cell pressures and $\bar{\boldsymbol{q}}_{\boldsymbol{cm}}$ is the vector of source terms corresponding to the matrix cells. G_{mm} and $\mathcal{G}_{mf}$ are matrices corresponding to the pressure unknowns for rock matrix and fracture cells respectively. $\mathcal{G}_{mf}$ is the coupling of matrix pressure unknowns with the pressure unknowns for connected fracture cells because of matrix-fracture fluxes as expressed in (13). Similarly, discrete approximation of the divergence equation (6) for a 2D fracture cell is written as;

$$\sum_{j=1}^{N_e}\sum_{k=1}^{2} \mathcal{F}_{j,k} + \sum_{j=1}^{N_e} Q_{f\,j} = \bar{q}_{cf} \quad \text{for every fracture cell} \tag{29}$$

where $\mathcal{F}_{j,k}$ is the fracture-fracture flux on sub-face k of the face (edge) j of the 2D surface fracture cell which consists of N_e number of faces (edges). For triangular fracture cells, in the 3D problem, there will be three faces (edges), each decomposed into two sub-faces, for every fracture cell. Q_f and $\bar{q}_{cf}$ are the transfer function and any known source term respectively for the corresponding fracture cell. Fracture-fracture fluxes are defined by (26). Because each fracture cell is common to two neighbouring clusters of matrix cells, so the total transfer function Q_f is determined by the addition of transfer functions of sub-cells determined via (21), from the corresponding clusters, in terms of matrix and fracture pressure unknowns. Using (26) and (29), the system of equations describing mass conservation in the fracture cells, can be written as;

$$G_{ff}\Phi_f + \boldsymbol{Q}_f = \bar{\boldsymbol{q}}_{cf} \tag{30}$$

where G_{ff} corresponds to the fracture-fracture fluxes, $\bar{\boldsymbol{q}}_{\boldsymbol{cf}}$ is the vector of known source terms for the fracture cells and $\boldsymbol{Q}_f$ is the vector of transfer functions corresponding to fracture cells. Using (21), equation (30) is expressed as

$$\begin{aligned} G_{ff}\Phi_f + \mathcal{G}_{Tm}\Phi_m + \mathcal{G}_{Tf}\Phi_f &= \bar{\boldsymbol{q}}_{cf} \\ \text{or} \quad (G_{ff} + \mathcal{G}_{Tf})\Phi_f + \mathcal{G}_{Tm}\Phi_m &= \bar{\boldsymbol{q}}_{cf} \end{aligned} \tag{31}$$

where $\mathcal{G}_{Tm}$ and $\mathcal{G}_{Tf}$ correspond to transfer functions for the fracture cells. $\mathcal{G}_{Tm}$ is the coupling between pressure unknowns for matrix and fracture cells.

Thus we have two systems to solve, (28) and (31), for unknown pressures in the matrix and fracture cells respectively, which combine to form the coupled linear system:

$$\begin{pmatrix} G_{mm} & \mathcal{G}_{mf} \\ \mathcal{G}_{Tm} & G_{ff} + \mathcal{G}_{Tf} \end{pmatrix} \begin{pmatrix} \Phi_m \\ \Phi_f \end{pmatrix} = \begin{pmatrix} \bar{\boldsymbol{q}}_{cm} \\ \bar{\boldsymbol{q}}_{cf} \end{pmatrix}$$

Using simplified notation where $\bar{G}_{ff} = G_{ff} + \mathcal{G}_{Tf}$, the system is then written as;

$$\begin{pmatrix} G_{mm} & \mathcal{G}_{mf} \\ \mathcal{G}_{Tm} & \bar{G}_{ff} \end{pmatrix} \begin{pmatrix} \Phi_m \\ \Phi_f \end{pmatrix} = \begin{pmatrix} \bar{\boldsymbol{q}}_{cm} \\ \bar{\boldsymbol{q}}_{cf} \end{pmatrix} \tag{32}$$

Matrix-matrix fluxes and matrix-fracture fluxes in (13) and fracture-fracture fluxes in (26) can be determined separately in parallel and assembled into the coupled linear system (32). Iterative solution methods can be used to solve (32) for matrix and fracture pressures. The performance and computational cost of iterative solution method is proportional to the condition number of the linear system to be solved. In our case, the condition number of the coupled linear system depends on the grid cell size, fracture aperture and fracture permeability. For certain grid cell size and fracture aperture, the higher the fracture permeability, the higher the condition number of the fracture-fracture system $\bar{G}_{ff}$, leading to an even higher condition number of the overall coupled linear system. Since the general global linear system (32) is non-symmetric (unless the mesh consists of uniform hexahedrons), so we solve the system via GMRES[41] method preconditioned by the algebraic multi-grid (AMG) [42] or incomplete-LU (iLU) by employing the library PETSc[43].

4. Transport model

We use an explicit first order upwind (upstream weighting) method for computing tracer transport. We treat the intersecting fractures in the same way as treated in [2] and [18]. The discrete transport equation for the fracture cell can be written as;

$$\varphi \frac{c^{n+1} - c^n}{\delta t} V_f + \sum_{j=1}^{N_e} \mathcal{F}_j c_{fo} - F_{m_1} c_1 - F_{m_2} c_2 = q_{cf} V_f \quad \text{for time step } n \tag{33}$$

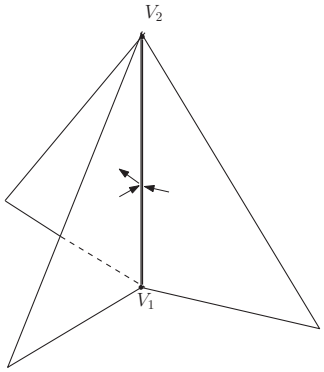

Figure 3: Intersecting fractures with line V_1V_2 as the intersection interface.

where, c is the concentration of the tracer in the fracture cell of volume V_f, $\mathcal{F}_j$ are the fracture-fracture fluxes, F_{m_1} and F_{m_2} are the matrix-fracture fluxes, outward normal to neighbouring matrix cells m_1 and m_2, as computed in previous section (expressions (8) and (9)). c_1 and c_2 are the concentration of a fracture cell or neighbouring matrix cell depending on the upstream direction of flux i.e. into the fracture or out of the fracture. c_{fo} is the concentration at the intersection line between the intersecting fracture cells; depicted by V_1V_2 in Fig. 3. We assume that the flow is fast in the fractures such that there is no accumulation of mass at the intersection line. If there are N intersecting fractures meeting at the line and there are l fluxes going into the intersection line then we can compute c_{fo} by the following condition;

$$\sum_{k=1}^{l} \mathcal{F}_k c_k = c_{fo} \sum_{k=1}^{N-l} \mathcal{F}_k \tag{34}$$

In this way we do not need to include the small intermediate cell explicitly, as in the equi-dimensional model, in overall computations and avoid the restriction of a low CFL condition that would result from inclusion of the intermediate cell.

5. Numerical results

Numerical results are presented in this section to assess and demonstrate the lower-dimensional fracture modelling by CVD-MPFA. First, we show a fracture-only simulation to show the application of the 2D CVD-MPFA formulation for surface fractures oriented in 3D. Then, we assess the accuracy of the lower-dimensional fracture model for a challenging discrete fracture-matrix problem and observe the effect of the ζ parameter in the discontinuous fracture pressure formulation. In the next sub-section we compare the pressure and tracer transport fields, for a discrete fracture-matrix system, computed by the lower-dimensional model and equi-dimensional fracture models respectively on unstructured meshes. We also discuss the complexity of the method with respect to the number of fractures and the characteristics of these. A test case is presented that involves simulation of a complex discrete fracture-matrix system for a slightly compressible fluid. We conclude this section with a study to analyse the sensitivity of the results on the grid resolution of matrix

and fractures.

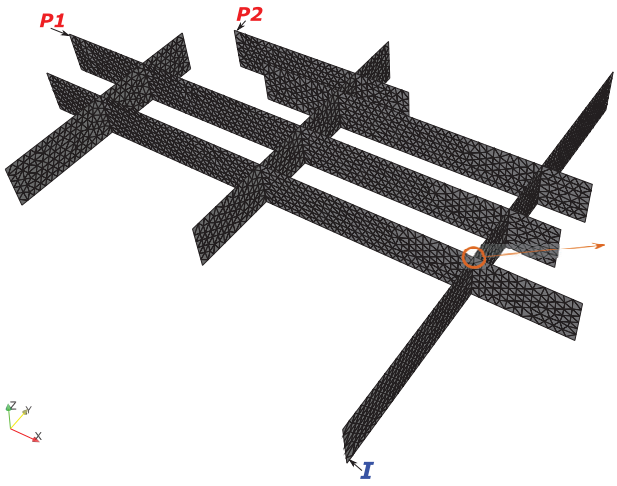

(a) Mesh of 3D volumetric fractures consists of 4716 thin prismatic cells and the mesh of 2D surface fractures consists of 4662 triangular cells. As both meshes are indistinguishable at this scale, only one mesh is shown.

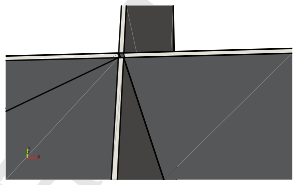

(b) Close-up view of the thin hexahedral intermediate cell at the intersection of thin 3D volumetric prism fracture cells

Figure 4: Fracture network mesh

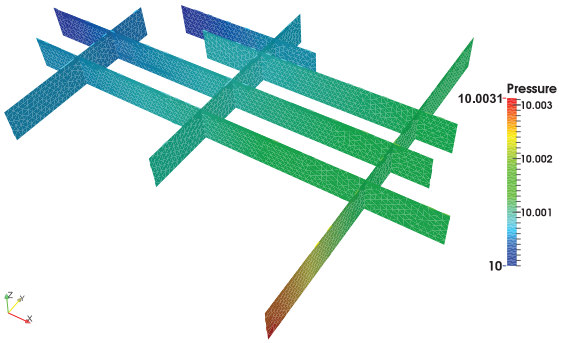

(a) Pressure field for 3D fractures

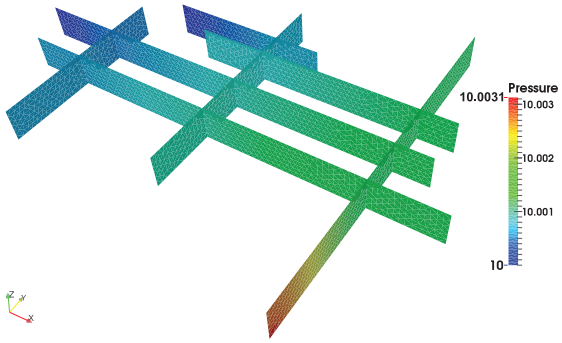

(b) Pressure field for the 2D fractures. L^2 relative error norm $= 6.115e-11$ when compared with the pressure field for the 3D fractures

Figure 5: Pressure fields for the 3D fractures and the 2D fractures

5.1. Fracture-only simulation

The first example involves application of the surface CVD-MPFA formulation for a fracture network and its comparison with the full 3D discretised volumetric fracture network. The fracture-network consists of 7 interconnected fractures which are 2D surfaces oriented in 3D space. The size of the whole system is $200 \times 150 \times 15$ m^3. We discretise the fracture surfaces with a conforming Delaunay mesh with lines (edges) at the intersection of the fracture surfaces. The corresponding 3D fracture network is discretised into a thin prismatic mesh of the same resolution as of the surface fractures. There are thin hexahedral cells at the junction of the intersecting 3D fractures. The fracture-network mesh and a thin hexahedral cell at one of

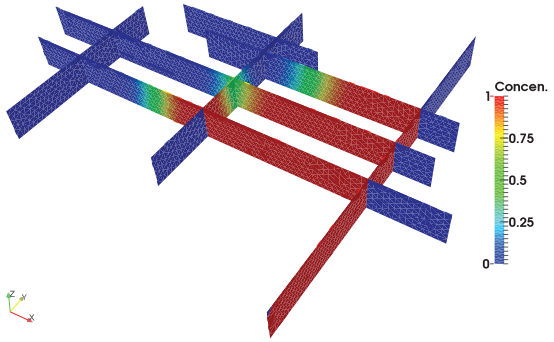

(a) Tracer concentration for 3D fractures at $t = 5.0$ years

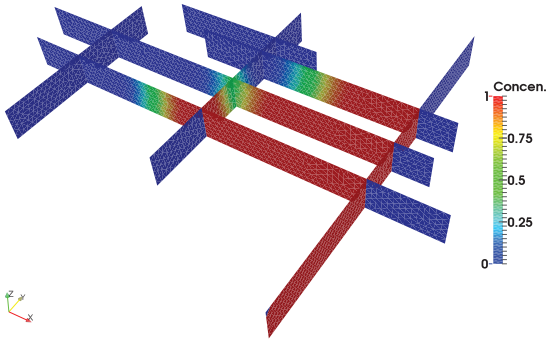

(b) Tracer concentration for 2D fractures at $t = 5.0$ years

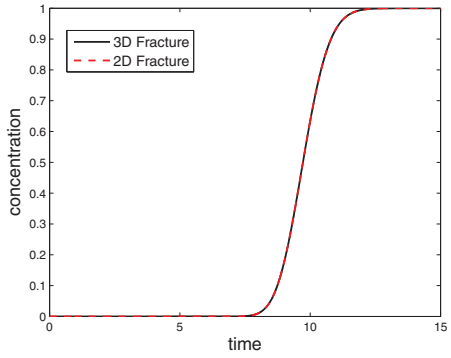

(c) Tracer concentration at producer *P1* w.r.t time (years). Concen. at producer *P1* at $t = 10$ years for 3D fractures is 0.634458 and for 2D fractures is 0.634431.

Figure 6: Tracer concentration plots for the 3D fractures and the 2D fractures

the intersections are shown in Fig. 4. All fractures are assigned an isotropic permeability of $\boldsymbol{K_f} = 10^6 \boldsymbol{I}$ mD. The aperture of each fracture is $a = 1$ mm. Fluid is injected through an injector I at the rate of $2.739e-3$ m^3/day and 10 bar pressure is imposed at producers *P1* and *P2*. Locations of injector and producers are depicted in Fig. 4. We solve the fracture-only equation (29) by the CVD-MPFA formulation presented in section 3.2 and ignore the transfer function because the matrix is absent in this case. The respective pressure fields computed using the 3D model and 2D surface fracture model are shown in Fig. 5. We note that the pressure field computed by the CVD-MPFA formulation for the 2D triangulated fracture surfaces is in excellent agreement with the pressure field computed by using the full 3D gridded volumetric fracture network, with an overall L^2 relative error of $6.115e-11$ difference between the respective pressure fields. The corresponding tracer concentration contours at $t = 5$ years are shown in Figs. 6b and 6b with similar excellent agreement. Plots of concentration versus time at producer *P1*, obtained by both models, are seen to overlap each other as shown in Fig. 6c.

5.2. Single fracture; Anisotropic discontinuous permeabilities and BCs

The next case involves a single fracture of anisotropic permeability, embedded in the matrix. The boundary conditions for the fracture and matrix are quite distinct and give rise to a discontinuity at the boundary

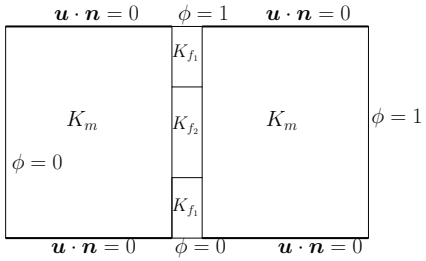

(a) 2D domain in XY

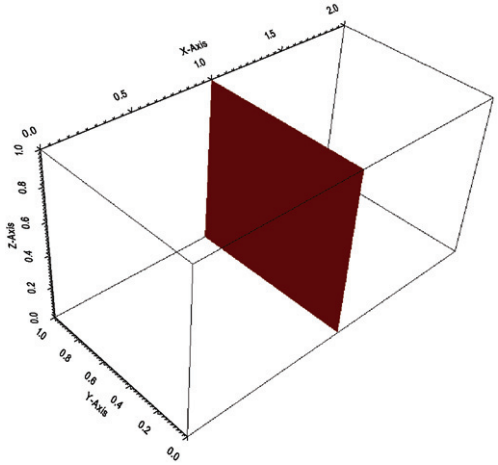

(b) 3D domain with a single surface fracture with heterogeneous permeability illustrated in Fig. 7c

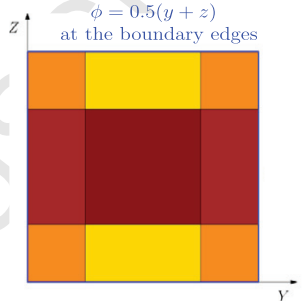

(c) Heterogeneity of surface fracture

Figure 7: Domain and boundary conditions for single fracture test

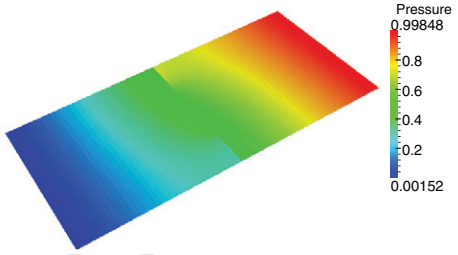

(a) 2D Pressure field

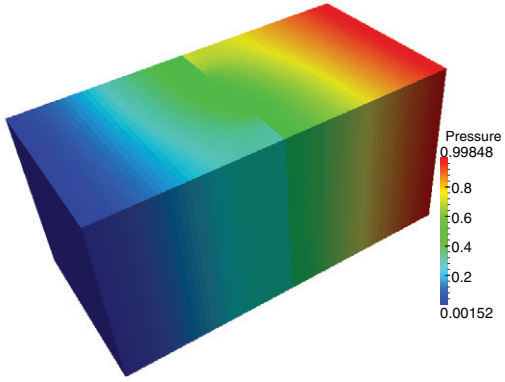

(b) 3D Pressure field

Figure 8: 2D and corresponding 3D Pressure fields for $k_f = 200$ and aperture, $a = 1e-2$ m.

surfaces. We assess the accuracy of the 2D fracture discontinuous pressure model and observe the influence of different values of parameter ζ.

First we solve the problem as the projected case of the 2D problem presented in [16, 37] to validate the 3D model and the implementation. The 2D domain is shown in Fig. 7a. Permeability of the rock-matrix is isotropic with $\boldsymbol{K}_m = \boldsymbol{I}$ mD, in contrast the fracture permeability is anisotropic and discontinuous with $\boldsymbol{K_{f1}} = \begin{pmatrix} 1/k_f & 0.0 \\ 0.0 & k_f \end{pmatrix}$ mD and $\boldsymbol{K_{f2}} = \begin{pmatrix} k_f & 0.0 \\ 0.0 & 1/k_f \end{pmatrix}$ mD where $k_f > 1.0$. Consequently fluid cannot flow along

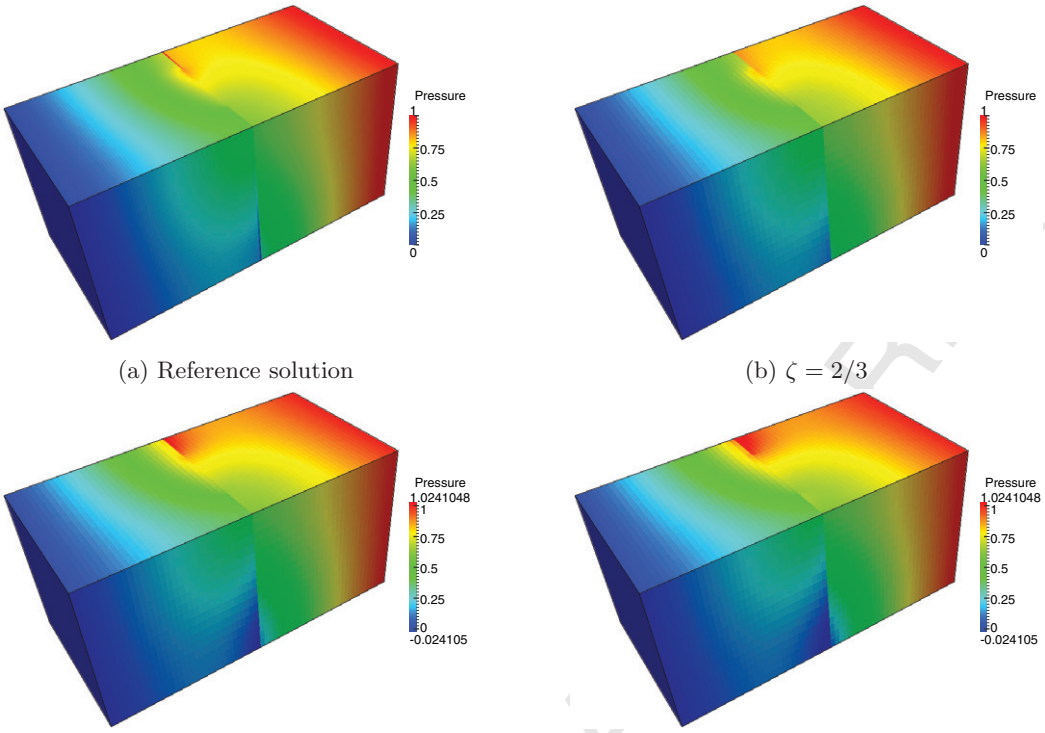

(a) Reference solution (b) $\zeta = 2/3$

(c) $\zeta = 0.51$ (d) $\zeta = 0.49$

Figure 9: Reference solution and the 2D fracture model Pressure field for fracture aperture, $a = 1e-2$ m and $k_f = 200$

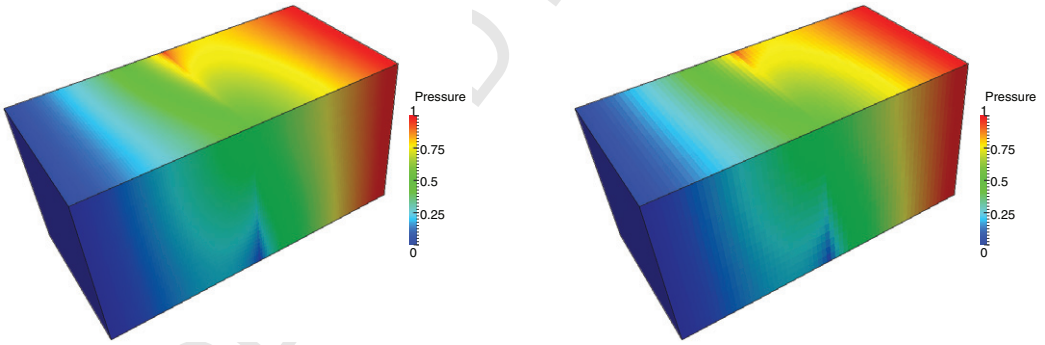

(a) Reference solution (b) $\zeta = 2/3$

Figure 10: Reference solution and the 2D fracture model Pressure field for fracture aperture, $a = 5e-4$ m and $k_f = 200$

the middle part of the fracture but can cross it. Dirichlet boundary conditions are applied at the ends of fracture. The 3D domain of size $[2 \times 1 \times 1]$ m^3 is shown in Fig. 7b and has the same permeability as discussed for the 2D domain along-with the $K_{zz} = 1.0$ mD in the fracture. A uniform structured quadrilateral mesh and hexahedral mesh are used for this test case in 2D and 3D respectively. The mesh cell size is $L_h = 1.0/32$ m. The pressure fields for the 2D and 3D domains, computed by lower-dimensional fracture model (with $\zeta = 2.0/3.0$), are shown in Fig. 8. The pressure fields for the 2D domain and the 3D domain plane view are identical as expected.

Now, we extend the 2D problem into a fully 3D problem and analyse the influence of different values of pa-

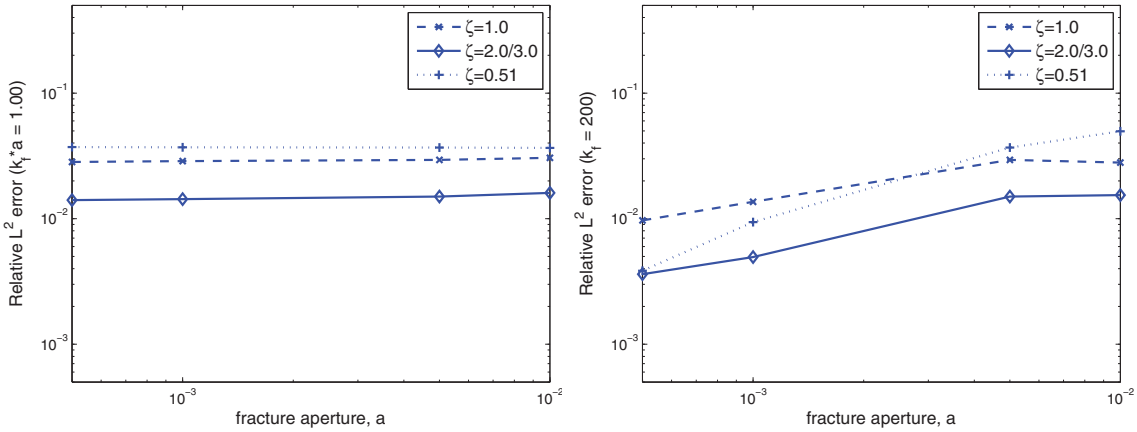

(a) $k_f * a = 1.0$ (b) $k_f = 200$

Figure 11: Relative L^2 error variation versus the fracture aperture. For 2D fracture model mesh has $64 \times 32 \times 16$ cells. Cell length, $L_h = 1/32$ m

rameter ζ on the accuracy of the 3D CVD-MPFA formulation coupled with a 2D fracture. The permeability of the matrix is defined by $\boldsymbol{K_m} = \boldsymbol{I}$ mD. The permeability of the fracture is given by;

$$\boldsymbol{K_f} = \begin{pmatrix} k_{xx} & 0.0 & 0.0 \\ 0.0 & k_{yy} & 0.0 \\ 0.0 & 0.0 & k_{zz} \end{pmatrix} \text{ mD}$$

(i) $k_{xx} = k_f, \quad k_{yy} = 1/k_f \quad \forall y \in [0.25, 0.75]$ m,

(ii) $k_{xx} = 1/k_f, \quad k_{yy} = k_f \quad \forall y \in [0, 0.25) \cup (0.75, 1]$ m

(iii) $k_{zz} = 1/k_f \ \forall z \in [0.25, 0.75]$ m and $k_{zz} = k_f \ \forall z \in [0, 0.25) \cup (0.75, 1]$ m.

where, $k_f > 1.0$.

Permeability definitions (i) and (ii) are the same as used for the 2D problem previously, while definition (iii) is for the z-direction. The heterogeneity of the fracture is depicted in Fig. 7c. The Dirichlet boundary conditions of $\phi = 0.0$ bar and $\phi = 1.0$ bar are imposed at the YZ surfaces of the matrix at $x = 0.0$ m and $x = 2.0$ m respectively. Zero flux is imposed on all other boundary surfaces of the matrix. The Dirichlet condition $\phi = 0.5(y + z)$ bar is imposed on all the boundary edges of the fracture. We solve the problem using the lower-dimensional model and assess its accuracy with respect to the parameter ζ of the model and fracture attributes (k_f, a). We compare with the reference solution obtained by the equi-dimensional method (CVD-MPFA, $q = 1.0$) using a much refined mesh. A uniform structured hexahedral mesh is used for this test case. The cell size of the mesh for the reference solution is $L_h^* \approx 1.0/64$ m and 3D fracture cell size is $L_{h,f}^* = a/3$ m in normal x-direction. The total number of cells is 268288. The mesh cell size for the 2D fracture model is $L_h = 1.0/32$ m and has a total of 32768 matrix cells and 512 2D fracture cells. Fig. 9 shows the reference pressure solution and the pressure field computed by the lower-dimensional fracture model with different values of parameter ζ for the fracture aperture $a = 1e-2$ m and $k_f = 200$. For the value $\zeta = 2.0/3.0$, the resulting pressure field is comparable to the reference solution. The pressure fields produced by $\zeta = 0.51$ and $\zeta = 0.49$ have spurious oscillations close to the fracture and violate the discrete maximum principle (DMP) so these values of ζ should be avoided for high aperture values. The same behaviour is observed for the 2D case in [16, 37]. Pressure fields for the fracture aperture $a = 5e-4$ m and $k_f = 200$ are

shown in Fig. 10. The accuracy of the 2D fracture model, with different values of parameter ζ with respect to the fracture aperture a and for k_f is shown in Fig. 11. The relative L^2 error of the pressure field is not affected by the change of aperture if $k_f * a = 1.0$ as shown in Fig. 11a but the pressure field behaviour changes with the change of parameter ζ of the model and we obtain the best accuracy for $\zeta = 2.0/3.0$. Fig. 11b shows the relative L^2 error versus fracture aperture for high permeability contrast with $k_f = 200$. For this case the relative L^2 error increases with increase of the aperture. For all the cases discussed here the 2D fracture model with $\zeta = 2.0/3.0$ yields the best solution accuracy.

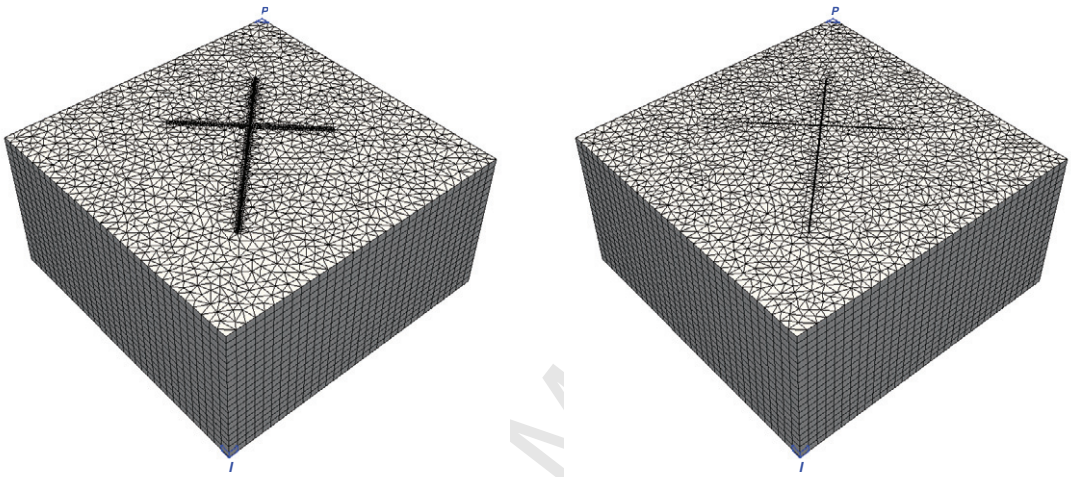

(a) 92440 3D cells (b) 63280 3D cells + 1420 2D fracture cells

Figure 12: (a) Explicit grid representation of intersecting fractures of aperture $a = 1$ mm and (b) mixed-dimensional grid with 2D fractures representation. Position of injector is marked by I and producer is marked by P.

5.3. Comparison of tracer transport: lower-dimensional versus 3D fracture model

We now solve the transport problems using fracture models (i) lower-dimensional fracture model (2D fracture) and (ii) equi-dimensional model (3D fracture) where fractures are gridded explicitly in the physical mesh. We solve the problem for a domain with two intersecting fractures. The same time step-size has been used for both the fracture models. We solve the problems with both variations of the 2D fracture model that are with continuous pressure and discontinuous pressure (with $\zeta = 2/3$) across the fracture and show contours of the solutions produced by the discontinuous pressure model as both give similar solutions for permeable fractures. We will refer to the discontinuous pressure model by *2D fracture* and continuous pressure model by *2D fracture-cont.* We compare the results of concentration variation with time at the producer. For the 3D fracture meshes, the whole domain is discretised by 3D prismatic cells including thin fractures. Moreover, the mesh is refined very close to the fracture to keep the quality of the mesh uniform. We solve the problem using CVD-MPFA. For the 2D fracture model, the fracture is treated as an internal boundary constraint and discretised by the specified quadrilateral faces of the 3D prismatic matrix cells. Grids for the test cases have been generated by the Triangle [44] unstructured mesh generator.

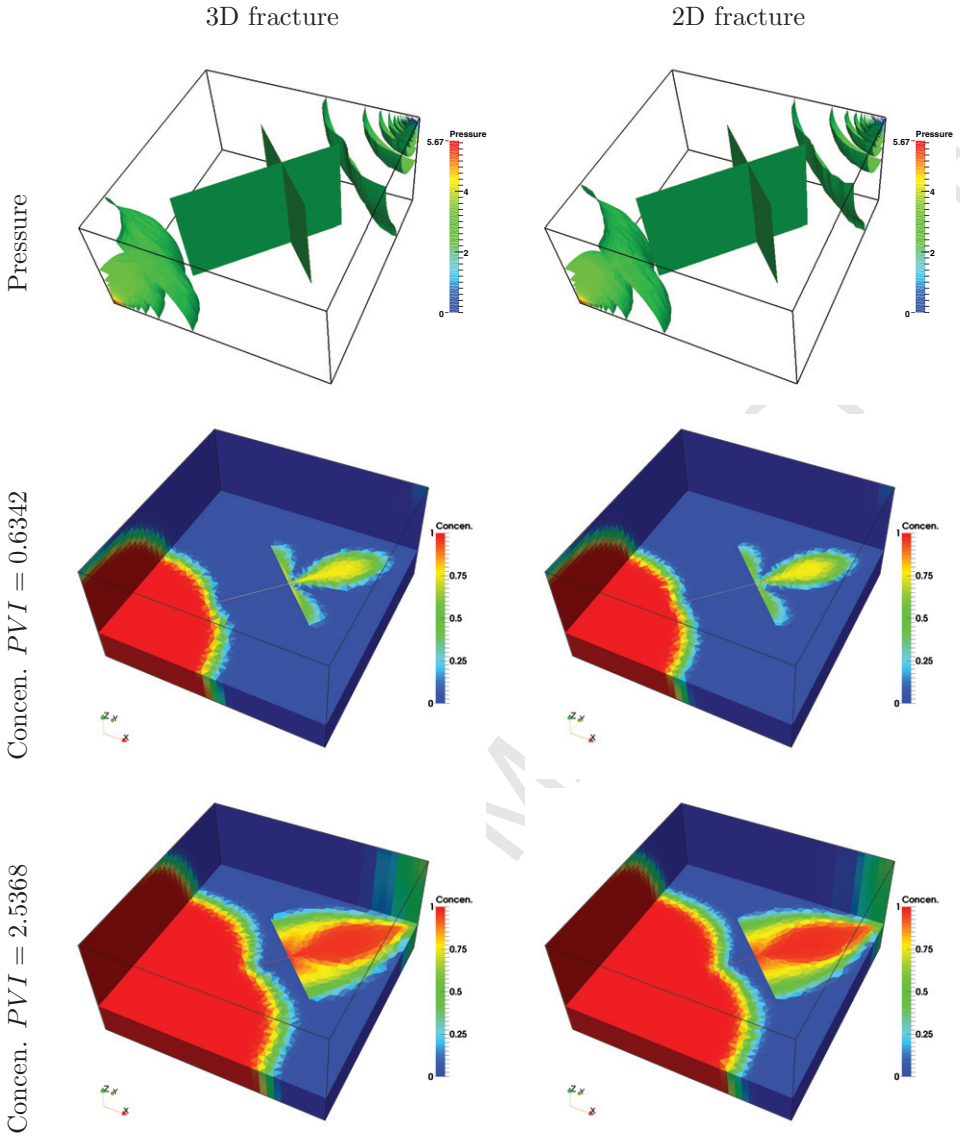

Figure 13: Pressure contours and tracer concentration contours at PVI= 0.6342 and PVI= 2.5368 computed by 3D fracture and 2D fracture model for isotropic permeability and $k_f = 10^4$.

The size of the domain is $1 \times 1 \times 0.5$ m^3. The meshes with explicit 3D fracture and 2D fracture representations are shown in Fig. 12. The aperture of both the fractures is $a = 1$ mm and two different permeability ratios are taken into consideration i.e. $k_f = 10^4$ and $k_f = 10^6$. Both fractures have the same permeability. Matrix permeability is defined by the identity tensor; $\boldsymbol{K}_m = \boldsymbol{I}$ mD for the first case. For the second case, an anisotropic permeability of ratio $10 : 5 : 1$ at an angle 30^o about $z - axis$ and $x - axis$ is used for $\boldsymbol{K}_m$. The fracture permeability is set to $\boldsymbol{K}_f = k_f \boldsymbol{K}_m$ for both isotropic and anisotropic cases. Zero-flux Neumann conditions are imposed on the whole external boundary of the domain. Fluid is injected through an injector I (with rate $1.7375e-3$ pore volumes per day) and pressure $\phi = 0$ bar is specified at the producer. Respective pressure and tracer concentration fields, produced by the two models are shown in Fig. 13 and Fig. 14,

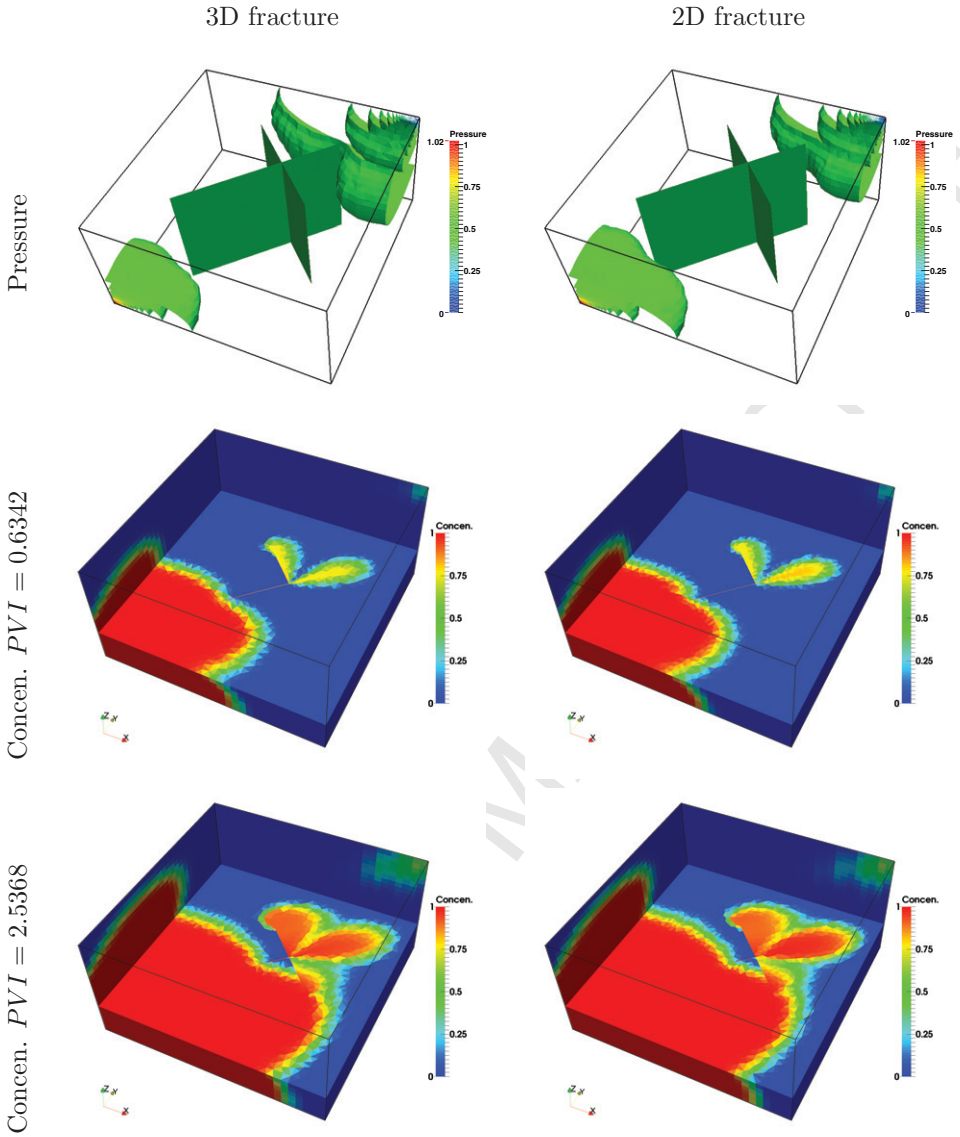

Figure 14: Pressure contours and tracer concentration contours at PVI= 0.6342 and PVI= 2.5368 computed by 3D fracture and 2D fracture model for anisotropic permeability and $k_f = 10^4$.

	Isotropic		Anisotropic	
Fracture model	$k_f = 10^4$	$k_f = 10^6$	$k_f = 10^4$	$k_f = 10^6$
3D fracture	29	24	55	54
2D fracture	7	7	7	7

Table 1: CPU times (sec) for the linear systems obtained by 3D and 2D fracture models. Linear systems are solved by GMRES preconditioned by algebraic multi-grid using PETSc.

with $k_f = 10^4$, for the cases of isotropic and anisotropic permeabilities respectively. Behaviour of solution contours are similar for $k_f = 10^6$ with overall good agreement between the 3D and 2D fracture models.

The CPU times necessary for solving the linear systems resulting from different permeability cases for 2D and 3D fractures are given in table 1. The CPU times are considerably lower for the 2D fractures as compared to

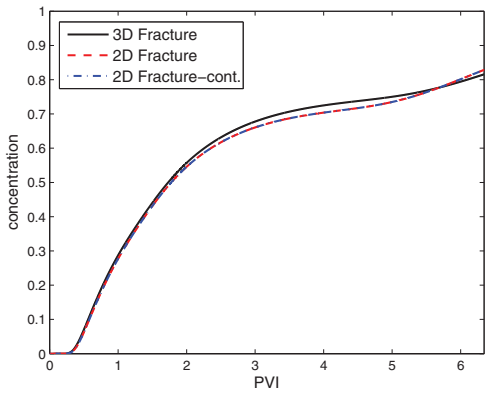

(a) Isotropic case

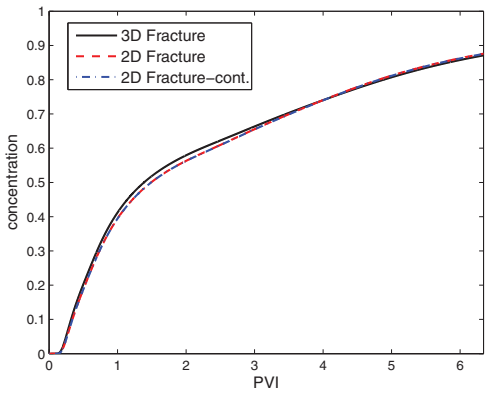

(b) Anisotropic case

Figure 15: Plots of tracer concentration at producer w.r.t time for permeability contrast $k_f = 10^4$.

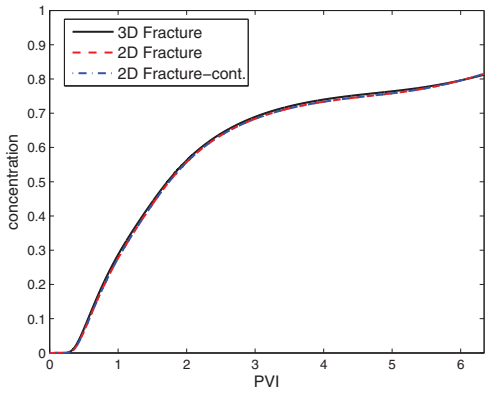

(a) Isotropic case

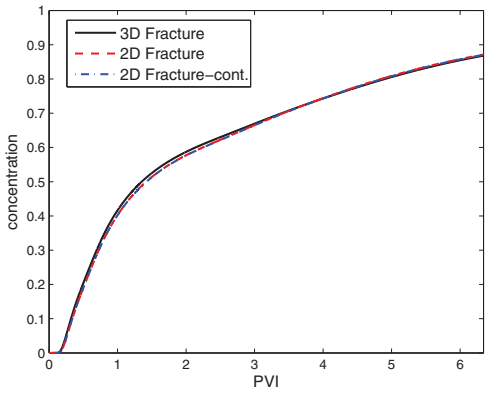

(b) Anisotropic case

Figure 16: Plots of tracer concentration at producer w.r.t time for permeability contrast $k_f = 10^6$.

the 3D fractures. Anisotropy of the problem increases the computational cost for the 3D fractures because of the change in the sparsity pattern of the linear systems. Whereas, there is no increase in the computational cost for 2D fractures with anisotropy because of the simpler fracture-matrix connections involving two-point fluxes. Moreover, tracer concentration at the producer is recorded for each time step.

The variation of tracer concentration at the producer with time computed by the two methods are shown in Figs. 15 and 16 for $k_f = 10^4$ and $k_f = 10^6$ respectively. The concentration plots show that the 2D fracture model yields results that are in excellent agreement with those of the 3D fracture model for high fracture permeability. While the lower permeability case proves more challenging with a partial discrepency in the concentration versus time profile, overall good agreement is obtained by the reduced dimensional model when compared to the explicit 3D fracture model. The 2D model yields comparable tracer transport results for higher permeable intersecting fractures. The treatment for intersecting fractures avoids the explicit representation of the small intermediate cell and associated small CFL number which is included in equi-dimensional model. Moreover, as shown in Figs. 15 and 16 the 2D fracture model with continuous pressure

across the fracture gives the results that are comparable to the results obtained by the discontinuous pressure model for the conductive fractures. The discrepancy between the two variations of the model is negligible for the isotropic case. We note that the discontinuous fracture pressure approximation is favourable when the fracture has low-permeability in the normal direction to the fracture.

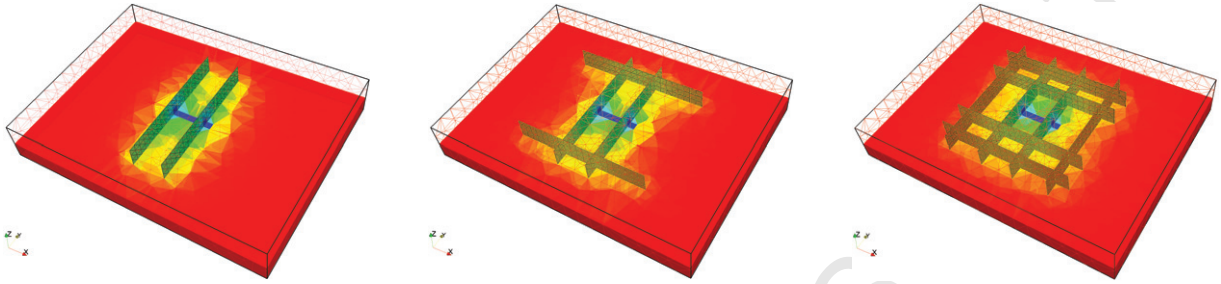

(a) Mesh 1: 2 fractures; 5141 tetrahedrons + 400 triangles; $\kappa = 1.82e7$

(b) Mesh 2: 4 fractures; 7453 tetrahedrons + 820 triangles; $\kappa = 1.11e7$

(c) Mesh 3: 8 fractures; 11593 tetrahedrons + 1700 triangles; $\kappa = 1.62e7$

Figure 17: Mesh specifications and the pressure fields for domains with different numbers of fractures with $k_f = 10^6$ and aperture $a = 1$ mm. Condition number κ is also given for each of the cases. There is a producer in the centre.

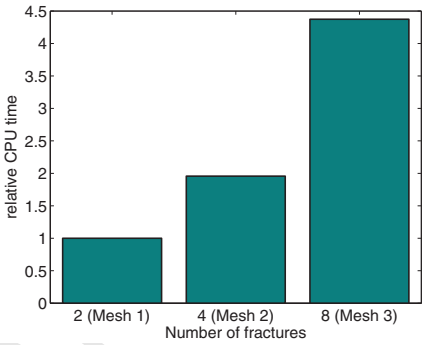

Figure 18: Computational cost to compute pressure fields for cases with different numbers of fractures ($k_f = 10^6$ and aperture $a = 1$ mm)

5.4. Complexity with respect to fracture characteristics

In this section, at first, we study the complexity of the method with increasing number of fractures in the network embedded in the matrix. We solve the steady-state pressure problem for three cases that have number of fractures of 2, 4 and 8, respectively, with the number of fractures increases by a factor of 2. We keep the fracture mesh size almost the same for all three cases so the number of fracture cells also increases by an approximate factor of 2. Since the tetrahedral matrix mesh conforms to the fractures, the number of matrix cells increases as the number of fracture cells increases. The Delaunay tetrahedral mesh is generated using Tetgen [45] using the default quality constraints. The domain size is $800 \times 600 \times 120$ m^3. There is a producer in the middle of the domain that produces at a pressure of 100 bar, while the external boundaries have an imposed pressure of 200 bar. Matrix permeability is defined by $\boldsymbol{K}_m = \boldsymbol{I}$ mD while the fractures are assigned a permeability of $\boldsymbol{K}_f = k_f \boldsymbol{K}_m$ where $k_f = 10^6$. The fracture aperture is $a = 1$ mm. Fig. 17 shows

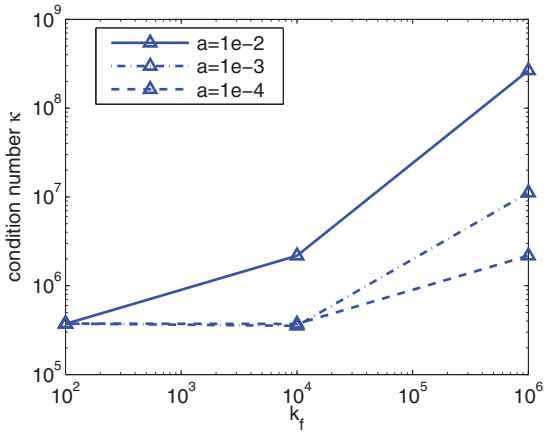

(a) Condition number w.r.t permeability ratio k_f and aperture a

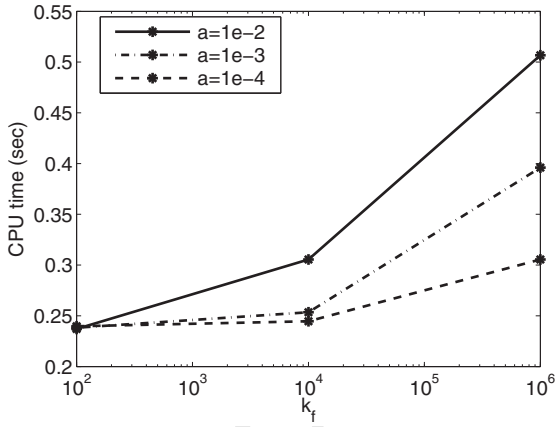

(b) CPU time w.r.t permeability ratio k_f and aperture a

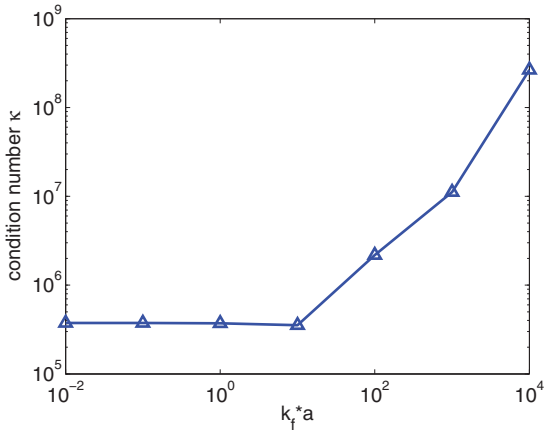

(c) Condition number w.r.t product of permeability ratio k_f and aperture a

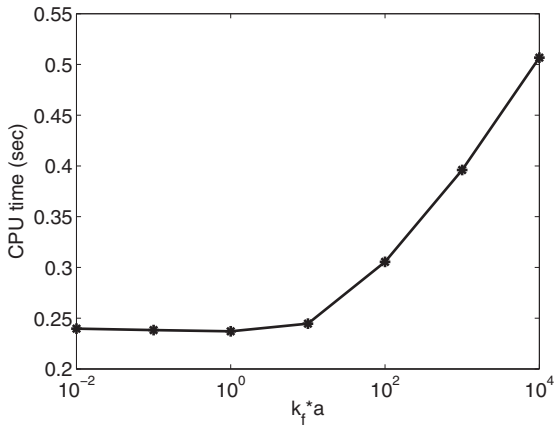

(d) CPU time w.r.t product of permeability ratio k_f and aperture a

Figure 19: Relationship between condition number and CPU time for the solution of the linear system w.r.t permeability ratio k_f and aperture a for Mesh 2 (Fig. 17b)

the meshes and the pressure fields for three cases that have different numbers of fractures. The condition number (κ) of each linear system is also shown. The order of magnitude of the condition number (κ) is the same for all three cases, showing the independence of the condition number on the number of fractures for a particular permeability and aperture. We employ the library PETSc (v 3.5.3) [43] for the solution of the global linear systems and execute computations on a machine with an Intel(R) Xeon(R) CPU E5-2687W v2 @3.40 GHz. We solve the linear system by GMRES preconditioned by iLU(0). The convergence criterion for the linear solver is the relative convergence tolerance of $1e-12$ (PETSc parameter *rtol*). The computational cost of solving the linear systems obtained for the three cases increases (by factor of 2), proportional to the number of fracture cells, as shown in Fig. 18.

Now, we analyse the relationship of condition number and computational cost with respect to the fracture permeability and the aperture for a fixed mesh and number of fractures. We compute the pressure field for

Mesh 2 (Fig. 17b) for different permeability ratios k_f and apertures a. Figs. 19a and 19b show that the condition number and the computational cost are high for the highly conductive fractures and increase with the increase in the fracture aperture. Figs. 19c and 19d show a clear relationship of both the condition number and computational cost with the product of permeability ratio and the aperture ($k_f * a$). The product $k_f * a$ is involved in the fracture-fracture flux formulation (Eq. (23)). With the increase in $k_f * a$, the condition number and the computational cost increase, directly proportional to the increase in $k_f * a$, for $k_f * a > 10$. For smaller values of this product ($k_f * a \leq 10$), the computational cost is mainly determined by the parameters that determine the matrix fluxes. Hence, the computational cost is basically constant for $k_f * a \leq 10$ for a fixed mesh and fixed matrix parameters.

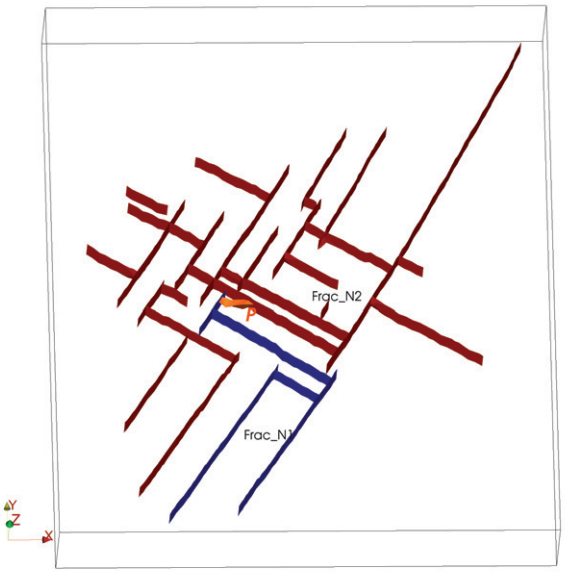

Figure 20: Domain consisting of matrix and fracture network. A producer is shown in the matrix between two sections of fracture network named 'Frac_N1' and Frac_N2.

5.5. 3D transient pressure simulation of realistic fractures

The final test case involves a 3D simulation of the discrete fracture-matrix system which includes complex intersecting fractures. We solve a transient pressure equation for a slightly compressible single phase-fluid, governed by

$$\varphi c_t \frac{\partial \phi}{\partial t} - \nabla \cdot \frac{\boldsymbol{k}}{\mu} \nabla \phi = q_c \tag{35}$$

where, φ is the porosity of domain and c_t is the total compressibility which is assumed constant here. The discrete form of Eq. (35), using (32), for the implicit scheme (in time), can be written as;

$$\begin{pmatrix} M_m + G_{mm} & \mathcal{G}_{mf} \\ \mathcal{G}_{Tm} & M_f + \bar{G}_{ff} \end{pmatrix} \begin{pmatrix} \Phi_m^{n+1} \\ \Phi_f^{n+1} \end{pmatrix} = \begin{pmatrix} \bar{\boldsymbol{q}}_{cm} + M_m \Phi_m^n \\ \bar{\boldsymbol{q}}_{cf} + M_f \Phi_f^n \end{pmatrix} \qquad \text{for time step } n \tag{36}$$

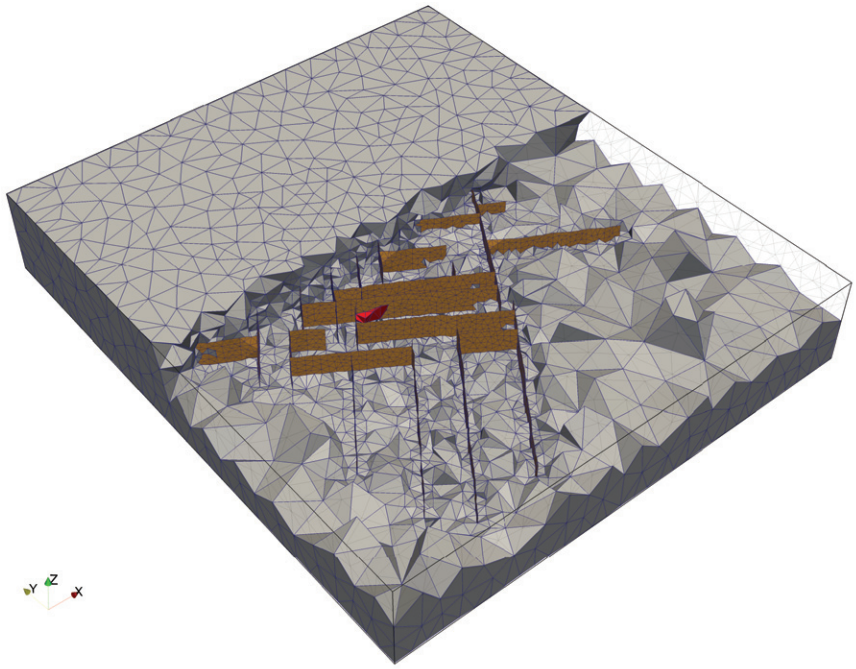

Figure 21: 3D conforming tetrahedral mesh for complex fractured domain where fractures are modelled as triangulated surfaces (55322 tetrahedrons + 5281 triangles).

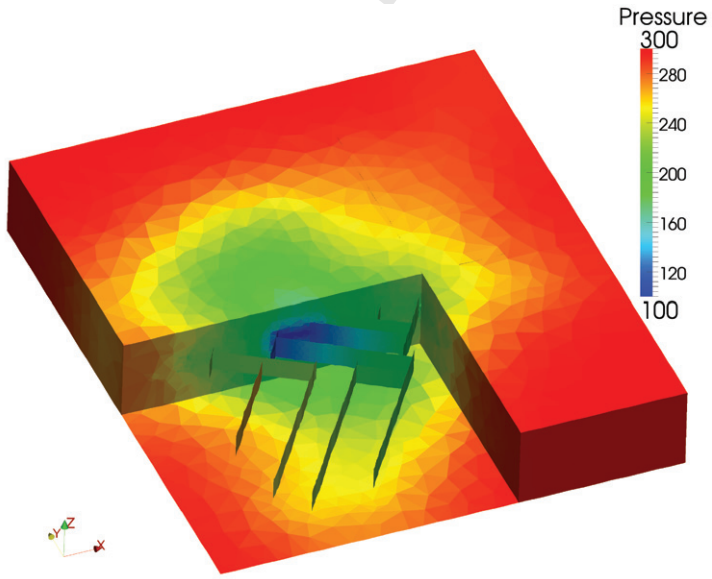

Figure 22: Pressure field after 18 days for the case of producer in the middle of domain with fracture network.

where, M_m and M_f are diagonal systems of coefficients $\varphi_m c_t/\delta t$, $\varphi_f c_t/\delta t$ associated with matrix and fracture respectively. The system size is $220 \times 240 \times 40$ m^3 and consists of 15 intersecting fracture surfaces. There is a producer in the middle of the domain between the sections of the fracture network named 'Frac_N1' and 'Frac_N2' in Fig. 20. The producer is intersecting both the sections of the fracture network which are

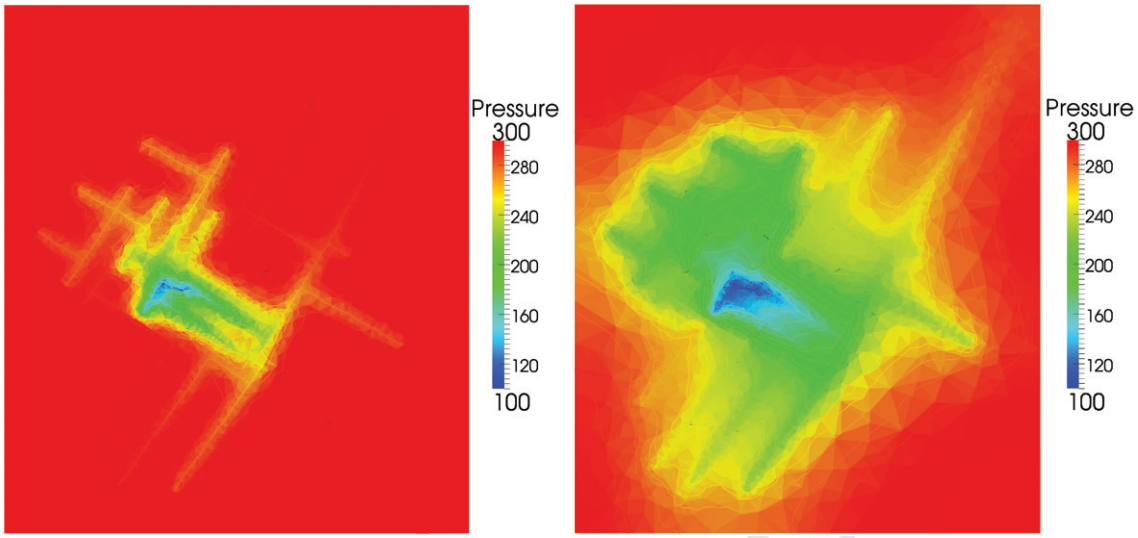

(a) 01 day

(b) 18 days

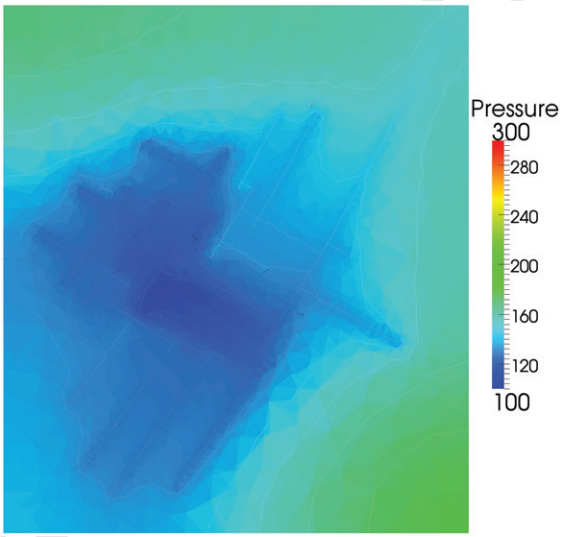

(c) 201 days

Figure 23: XY cross-section of the (transient) pressure contours at three different times.

otherwise not interconnected with each other. The producer has a constant pressure of 100 bar. The initial reservoir pressure is 300 bar. We discretise the whole domain in a conforming unstructured tetrahedral mesh with fractures defined by triangular internal-faces between the tetrahedrons. A fracture conforming 3D mesh is generated using Tetgen [45]. The mesh is depicted in Fig. 21. Matrix permeability is defined by the identity tensor; $\boldsymbol{K}_m = \boldsymbol{I}$ mD and porosity ($\varphi_m = 0.2$). Fracture permeability is set to $\boldsymbol{K}_f = 10^6 \boldsymbol{K}_m$ and porosity ($\varphi_f = 1.0$). All fractures are assigned aperture of $a = 1$ mm. We have assumed here a constant total compressibility ($c_t = 10^{-3}$ bar^{-1}) everywhere in the domain. Zero-flux Neumann conditions are imposed on the whole external boundary of the domain.

The pressure field is shown in Fig. 22 after 18 days of production. There is a high pressure gradient around the producer because of the presence of the highly conductive fracture network in the domain. Also, the

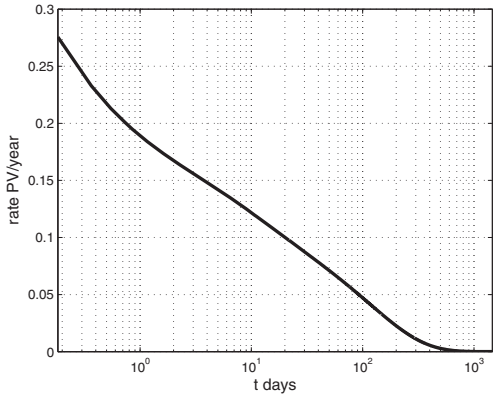

Figure 24: Production rate for the transient pressure field over the domain involving discrete fracture-matrix system for a period of 4 years.

pressure contours are non-symmetric and show anisotropy because of fractures. The production rate with respect to time is shown in Fig. 24 which shows the declining trend of the production rate. There is sharper decline of the production rate in the beginning than for the later stages. Cross-sections (XY) of pressure contours for the transient problem are shown in Fig. 23 at three different times. The pressure contours
505 illustrate (i) the depletion from the fracture network in the initial stage (ii) the matrix to fracture feed and (iii) the approach to the state where the pressure wave propagates into the fracture network which acts as the pressure boundary condition draining the surrounding matrix volume. This test case demonstrates the applicability of the presented method for the multi-rate aspects of drainage of a fractured zone involving a complex fracture network.

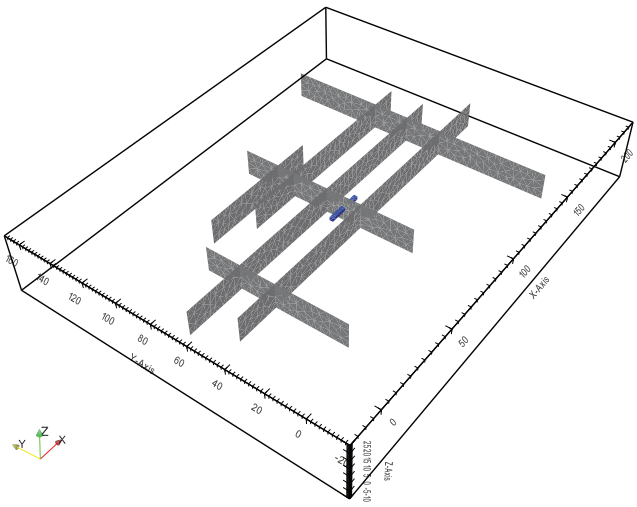

Figure 25: Domain with a fracture network for the grid sensitivity study. A producer in the middle is depicted as a blue horizontal tube extending in the x-direction.

Mesh name	No. of Matrix tetrahedrons	No. of fracture triangles
$Mat_1 - Frac_0$	59791	1618
$Mat_1 - Frac_1$	69451	1873
$Mat_1 - Frac_2$	79729	2432
$Mat_1 - Frac_3$	118148	5276
$Mat_1 - Frac_4$	176745	8709
$Mat_1 - Frac_5$	261074	14936
$Mat_1 - Frac_6$	402109	25299
$Mat_2 - Frac_4$	220127	8630
$Mat_3 - Frac_4$	318499	8788

Table 2: Specifications of the meshes used for the grid sensitivity study. Meshes are named by $Mat_i - Frac_j$ where Mat_i represents the tetrahedral matrix mesh refinement level and the $Frac_j$ represents the triangular fracture mesh refinement level

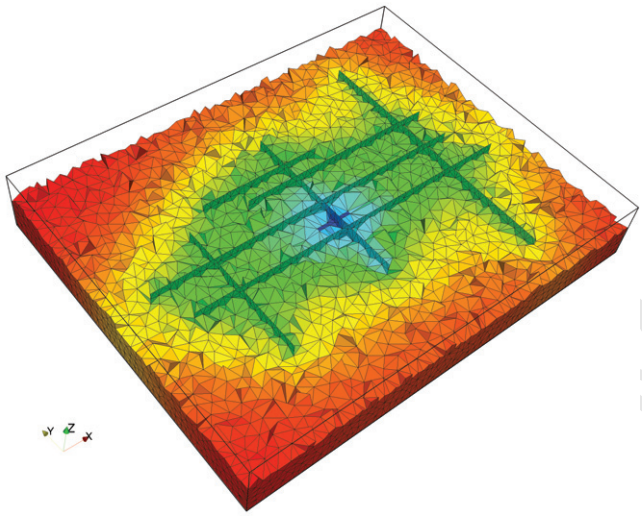

(a) $Mat_1 - Frac_0$

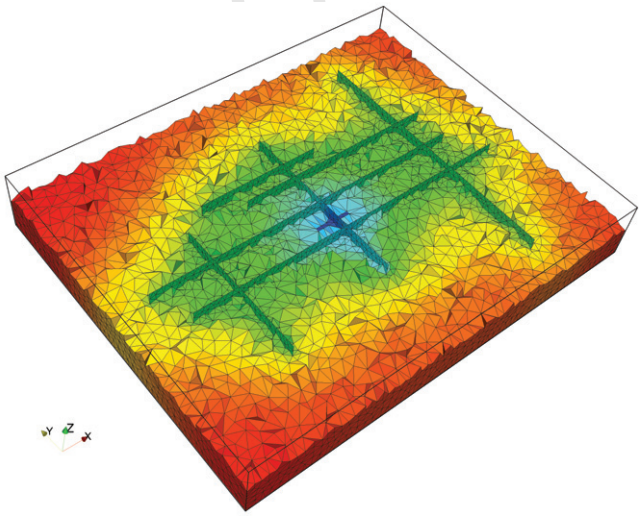

(b) $Mat_1 - Frac_2$

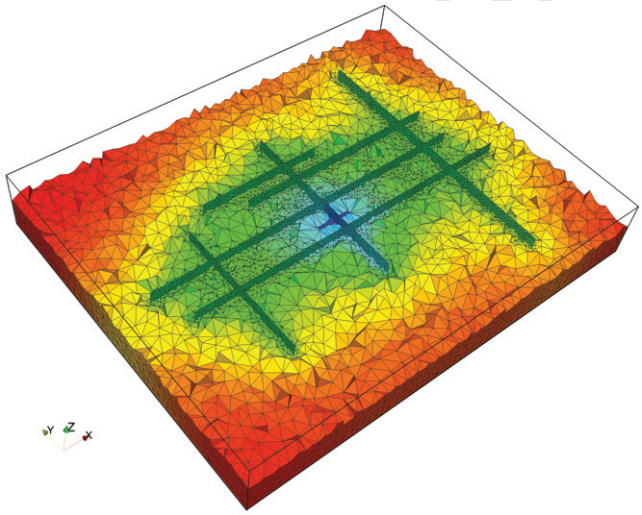

(c) $Mat_1 - Frac_4$

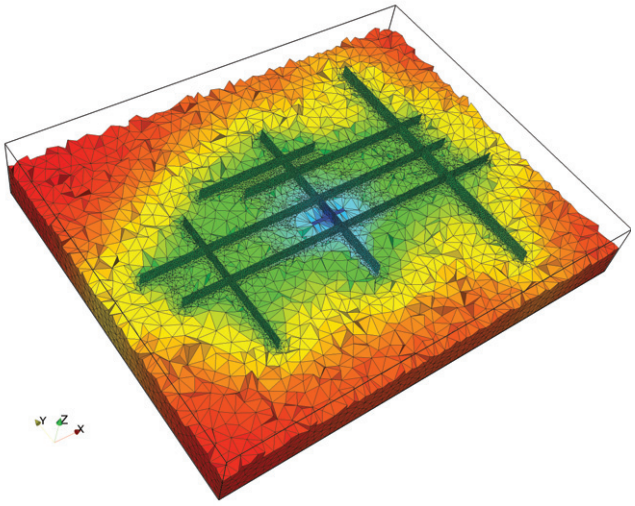

(d) $Mat_1 - Frac_6$

Figure 26: Meshes with increasing levels of local refinement of the fracture mesh and around the fractures

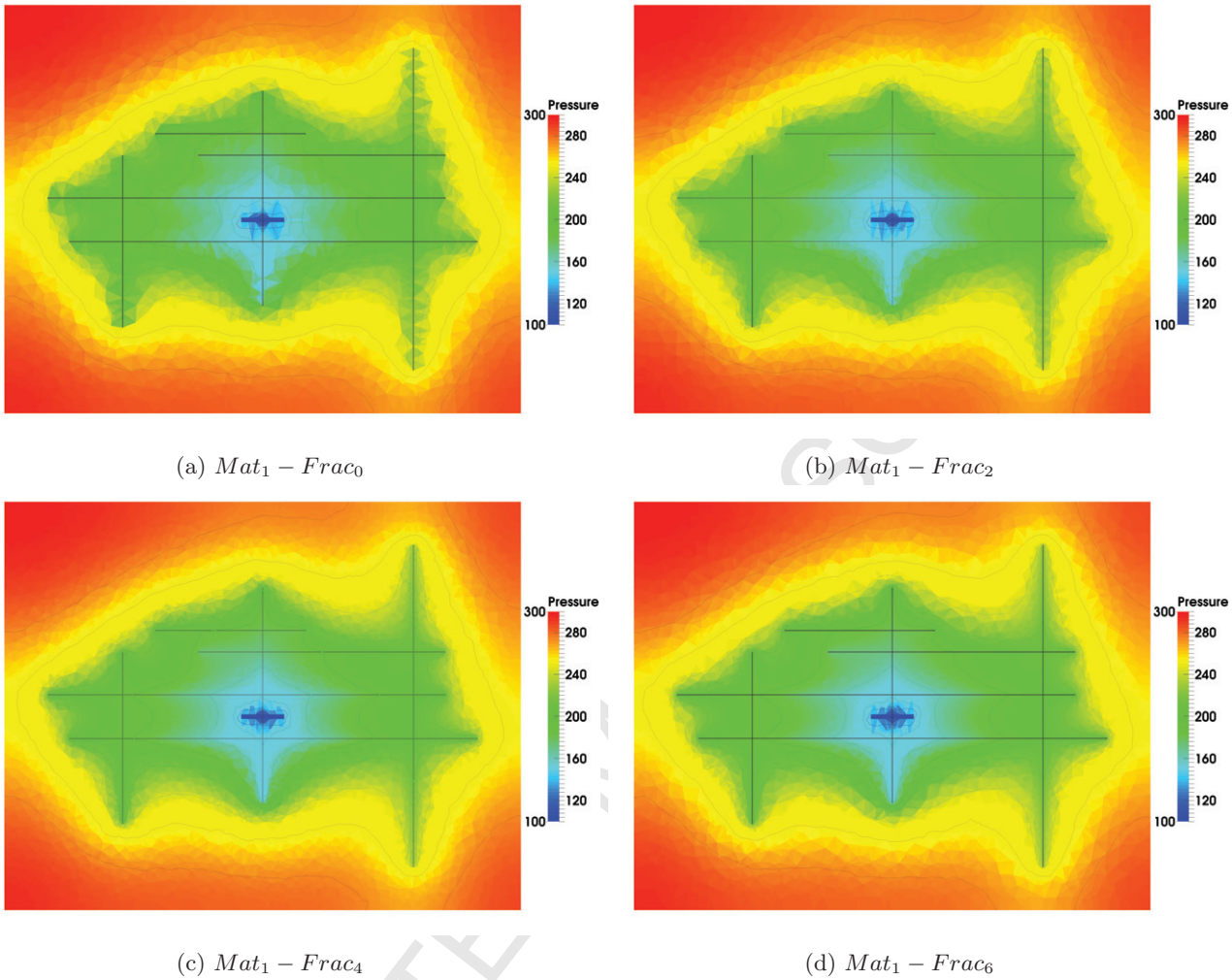

(a) $Mat_1 - Frac_0$

(b) $Mat_1 - Frac_2$

(c) $Mat_1 - Frac_4$

(d) $Mat_1 - Frac_6$

Figure 27: XY cross-sections of the pressure fields at $t = 18.25$ days for several meshes, with increasing levels of local refinement of the fracture mesh and around the fractures

5.6. Grid sensitivity study

In this section, we analyse the sensitivity of the transient pressure field with respect to the matrix and fracture mesh resolution. We solve the transient pressure problem similar to the case presented in the previous sub-section. There is a producer (of length 20 m) in the middle of the domain intersecting with the fracture network as shown in Fig. 25. The problem specifications are the same as given in the previous sub-section. We solve the problem using various meshes that have a different fracture and matrix mesh resolution, keeping the mesh size constant in and around the producer. The specifications of the meshes are given in table 2. Fig. 26 shows the meshes with increasing fracture mesh resolution and fixed matrix mesh size away from the fractures i.e. $Mat_1 - Frac_j$ from table 2, where $j = 0, \ldots, 6$. The corresponding cross-sections (XY) of the pressure fields are shown in Fig. 27. The solutions are consistent across the different mesh sizes. The production rates with respect to time for different fracture mesh resolutions are given in Fig. 29a. There is a difference in the production rates for different meshes in the initial period of

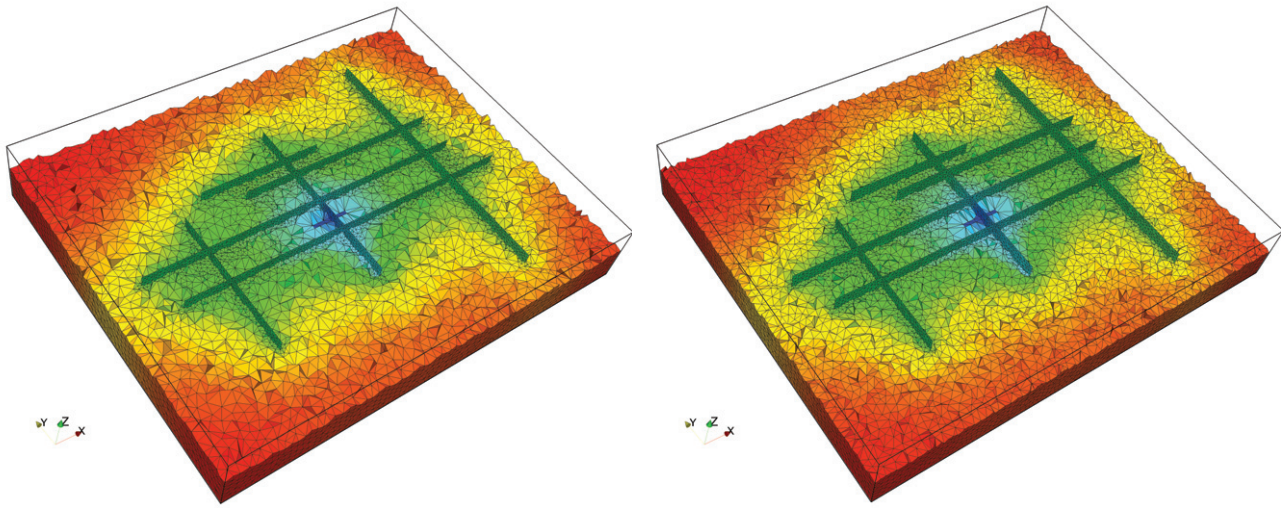

(a) $Mat_2 - Frac_4$ (b) $Mat_3 - Frac_4$

Figure 28: Meshes with increasing levels of refinement of the matrix mesh away from the fractures

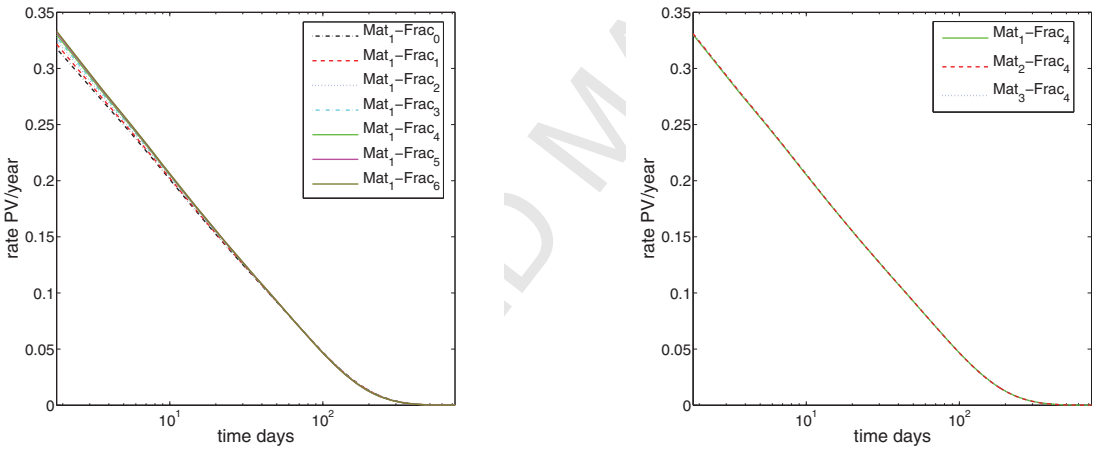

(a) Production rate for several meshes with increasing levels of refinement of the fracture mesh

(b) Production rate for several meshes with increasing levels of refinement of the matrix mesh

Figure 29: Production rate w.r.t time for different meshes.

production. Progressively refining the mesh of the fractures and thereby the mesh of the matrix close to the fractures improves the short term production profile until mesh $Mat_1 - Frac_4$. Further refinement does not yield further improvement of the solution.

Now, we analyse the sensitivity of the results with respect to the matrix mesh refinement away from fractures and keeping the fracture mesh resolution fixed. The transient problem is solved for the meshes $Mat_i - Frac_4$; $i = 1, 2, 3$ as shown in Figs. 26c and 28. The production rates for different levels of matrix mesh refinement, shown in Fig. 29b, overlap each other which depicts the independence of the results with respect to the matrix mesh resolution for this transient pressure problem with fixed time step size. The effect of the difference in time step size on the production rate is shown in Fig. 30 for a fixed mesh. Similar trends in the

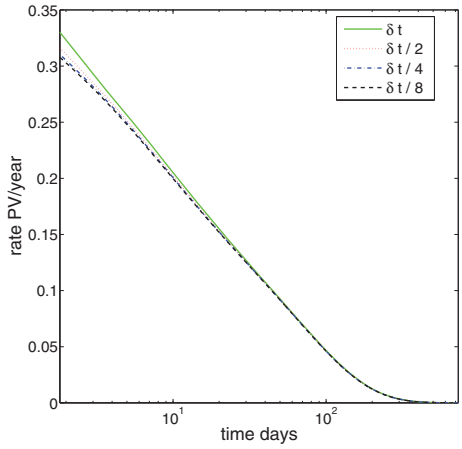

Figure 30: Production rate w.r.t time for different time step sizes, for the fixed mesh $Mat_1 - Frac_4$. $\delta t = 1.825$ days

results obtained using local grid refinement around fractures and global refinement through out the matrix verify that the CVD-MPFA formulation coupled with local grid refinement is advantageous and applicable to fracture modelling.

6. Conclusions

We have presented a CVD-MPFA formulation for discrete fracture-matrix simulations, in three-dimensions, where lower-dimensional fracture networks are efficiently coupled via a novel surface CVD-MPFA formulation for fractures. We compare pressure and transport results obtained by the lower-dimensional fracture model and equi-dimensional model on unstructured meshes. For thin highly conductive fractures, the lower-dimensional fracture model with continuous pressure approximation across the fracture yields results that are comparable to those of the explicit equi-dimensional modelling of fractures. We note that the lower dimensional model does not use extra matrix-fracture interfaces, thus reducing the local degrees of freedom. For problems involving systems of thin highly conductive fractures, we recommend using the lower-dimensional fracture model with continuous pressure approximation. Problems involving barriers are modelled by the lower-dimensional model with discontinuous pressure approximation. Numerical tests show that the lower-dimensional model with discontinuous pressure across the fracture yields improved flow resolution with minimum error when $\zeta = 2.0/3.0$ is used in the model.

We also present a tracer flow solver that is coupled with the respective 3D and surface fracture velocity fields and is used to assess the performance of the fracture model, the lower-dimensional results demonstrate the benefit of the method. The increase in complexity of the method with the increase of the number of fractures in the domain is also analysed. Furthermore, we present a transient pressure simulation, for a more complex discrete fracture-matrix system, which demonstrates the applicability of the method for multi-rate aspects of drainage of a fractured zone. A sensitivity study of the results obtained from a transient pressure problem with respect to matrix and fracture grid resolution, and time step size is also presented. Condition

numbers and CPU times are presented. The comparison with the equi-dimensional model shows that the lower-dimensional model provides a significant reduction in CPU time.

Acknowledgements

We thank Shell Global Solutions International B.V., Rijswijk, the Netherlands, for the financial support for this work, and for supplying fracture test data.

Nomenclature

CVD-MPFA	control-volume distributed multi-point flux approximation
DFM	discrete-fracture model
ϕ	pressure
$\boldsymbol{k}$	permeability tensor
μ	viscosity
$\boldsymbol{K}$	$\frac{\boldsymbol{k}}{\mu}$
a	fracture aperture
c_t	total compressibility
φ	porosity
c	tracer concentration
Φ	vector of pressures
F	matrix flux
$\mathcal{F}$	fracture-fracture flux
Q_f	transfer function
ζ	parameter for discontinuous pressure fracture-model

Subscripts

m	matrix
f	fracture

References

[1] S. K. Matthäi, Modelling multiphase flow in fractured porous rock, Tech. rep., Department of Earth Sciences & Engineering, Imperial College London (2005).

[2] H. Hoteit, A. Firoozabadi, An efficient numerical model for incompressible two-phase flow in fractured media, Adv. Water Resour. 31 (06) (2008) 891–905.

[3] L. H. Reiss, The reservoir engineering aspects of fractured formations, illustrated Edition, Editions Technip, Paris, 1980.

[4] J. Erhel, J.-R. D. Dreuzy, B. Poirriez, Flow simulation in three-dimensional discrete fracture networks., SIAM J. Sci. Comput. 31 (04) (2009) 2688–2705.

[5] B. Berkowitz, Characterizing flow and transport in fractured geological media: A review, Adv. Water Resour. 25 (2002) 861–884.

[6] J. E. P. Monteagudo, A. Firoozabadi, Control-volume method for numerical simulation of two-phase immiscible flow in two- and three-dimensional discrete-fractured media, Water Resour. Res. 40 (07) (2004) W074051–W0740520, http://dx.doi.org/10.1029/2003WR002996.

[7] G. Barenblatt, Y. Zheltov, I. Kochina, Basic concepts in the theory of seepage of homogeneous fluids in fissurized rocks, PMM 24 (05) (1960) 852–864.

[8] J. Warren, P. Root, The behavior of naturally fractured reservoirs, SPE J. 03 (03) (1963) 245–255.

[9] H. Kazemi, L. S. Merrill, K. L. Porterfield, P. R. Zeman, Numerical simultion of water-oil flow in naturally fractured reservoirs, SPE J. 16 (06) (1976) 317–326.

[10] Z. Chen, G. Huan, Y. Ma, Computational Methods for Multiphase Flows in Porous Media, Computational Science and Engineering, SIAM, Philadelphia, 2006.

[11] J. Noorishad, M. Mehran, An upstream finite element method for solution of transient transport equation in fractured porous media, Water Resour. Res. 18 (03) (1982) 588–596.

[12] R. Baca, R. Arnett, D. Langford, Modeling fluid flow in fractured porous rock masses by finite element techniques, Int. J. Numer. Methods Fluids 04 (04) (1984) 337–348.

[13] M. F. Lough, S. H. Lee, J. Kamath, An efficient boundary integral formulation for flow through fractured porous media, J. Comput. Phys. 143 (2) (1998) 462–483.

[14] M. Karimi-Fard, A. Firoozabadi, Numerical simulation of water injection in fractured media using the discrete-fracture model and the galerkin method, SPE Reserv. Eval. Eng. 6 (02) (2003) 117–126.

[15] S. K. Matthäi, A. Mezentsev, M. Belayneh, Control-volume finite-element two-phase flow experiments with fractured rock represented by unstructured 3D hybrid meshes, in: SPE Reservoir Simulation Symposium, Society of Petroleum Engineers, SPE, 2005.

[16] V. Martin, J. Jaffré, J. E. Roberts, Modelling fractures and barriers as interfaces for flow in porous media, SIAM J. Sci. Comput. 26 (2005) 1667–1691.

[17] H. Hægland, A. Assteerawatt, H. K. Dahle, G. T. Eigestad, R. Helmig, Comparison of cell- and vertex-centered discretization methods for flow in a two-dimensional discrete-fracture-matrix system, Adv. Water Resour. 32 (12) (2009) 1740–1755.

[18] T. H. Sandve, I. Berre, J. M. Nordbotten, An efficient multi-point flux approximation method for discrete fracture-matrix simulations, J. Comput. Phys. 231 (09) (2012) 3784–3800.

[19] B. T. Mallison, M. H. Hui, W. Narr, Practical gridding algorithms for discrete fracture modeling workflows, in: 12th European Conference on the Mathematics of Oil Recovery, EAGE, 2010.

[20] H. Mustapha, R. Dimitrakopoulos, T. Graf, A. Firoozabadi, An efficient method for discretizing 3D fractured media for subsurface flow and transport simulations, Int. J. Numer. Methods Fluids 67 (5) (2011) 651–670.

[21] H. Hajibeygi, Iterative multiscale finite volume method for multiphase flow in porous media with complex physics, Ph.D. thesis, ETH Zurich (2011).

[22] S. H. Lee, M. F. Lough, C. L. Jensen, Hierarchical modeling of flow in naturally fractured formations with multiple length scales, Water Resour. Res. 37 (03) (2001) 443–455.

[23] H. Hajibeygi, D. Karvounis, P. Jenny, A hierarchical fracture model for the iterative multiscale finite-volume method, J. Comput. Phys. 230 (24) (2011) 8729–8743.

[24] C. D. Foster, T. M. Nejad, Embedded discontinuity finite element modeling of fluid flow in fractured porous media, Acta Geotechnica 8 (1) (2013) 49–57.

[25] C. D'Angelo, A. Scotti, A mixed finite element method for Darcy flow in fractured porous media with non-matching grids, ESAIM: Math. Model. Numer. Anal. 46 (2012) 465–489.

[26] S. Berrone, S. Pieraccini, S. Scialò, An optimization approach for large scale simulations of discrete fracture network flows, J. Comput. Phys. 256 (2014) 838–853.

[27] A. Fourno, C. Grenier, A. Benabderrahmane, F. Delay, A continuum voxel approach to model flow in 3D fault networks: A new way to obtain up-scaled hydraulic conductivity tensors of grid cells, J. Hydrol. 493 (2013) 68–80.

[28] B. Noetinger, N. Jarrige, A quasi steady state method for solving transient Darcy flow in complex 3D fractured networks, J. Comput. Phys. 231 (1) (2012) 23–38.

[29] V. V. Mourzenko, I. I. Bogdanov, J.-F. Thovert, P. M. Adler, Three-dimensional numerical simulation of single-phase transient compressible flows and well-tests in fractured formations, Math. Comput. Simul. 81 (10) (2011) 2270–2281.

[30] M. Karimi-Fard, L. J. Durlofsky, K. Aziz, An efficient discrete-fracture model applicable for general-purpose reservoir simulators, SPE J. 09 (02) (2004) 227–236.

[31] A. Zidane, A. Firoozabadi, An efficient numerical model for multicomponent compressible flow in fractured porous media, Adv. Water Resour. 74 (2014) 127–147.

[32] K. Brenner, M. Groza, C. Guichard, R. Masson, Vertex approximate gradient scheme for hybrid dimensional two-phase Darcy flows in fractured porous media, ESAIM: Math. Model. Numer. Anal. 49 (2) (2015) 303–330. doi:10.1051/m2an/2014034.

[33] O. Al-Hinai, S. Srinivasan, M. F. Wheeler, Mimetic finite differences for flow in fractures from microseismic data, in: SPE Reservoir Simulation Symposium, Society of Petroleum Engineers, 2015.

[34] H. A. Friis, M. G. Edwards, J. Mykkeltveit, Symmetric positive definite flux-continuous full-tensor finite-volume schemes on unstructured cell-centered triangular grids, SIAM J. Sci. Comput. 31 (02) (2008) 1192–1220.

[35] M. Pal, M. G. Edwards, A family of multi-point flux approximation schemes for general element types in two and three dimensions with convergence performance, Int. J. Numer. Methods Fluids 69 (11) (2012) 1797–1817.

[36] R. Ahmed, M. G. Edwards, S. Lamine, B. A. H. Huisman, M. Pal, Mixed-dimensional model; CVD-MPFA coupled with a lower-dimensional fracture model, in: 14th European Conference on the Mathematics of Oil Recovery, EAGE, 2014.

[37] R. Ahmed, M. G. Edwards, S. Lamine, B. A. H. Huisman, M. Pal, Control-volume distributed multi-point flux approximation coupled with a lower-dimensional fracture model, J. Comput. Phys. 284 (2015) 462–489.

[38] F. Heße, V. Prykhodko, S. Attinger, Assessing the validity of a lower-dimensional representation of fractures for numerical and analytical investigations, Adv. Water Resour. 56 (2013) 35–48.

[39] V. Reichenberger, H. Jakobs, P. Bastian, R. Helmig, A mixed-dimensional finite volume method for two-phase flow in fractured porous media, Adv. Water Resour. 29 (07) (2006) 1020–1036.

[40] M. Pal, Families of control-volume distributed multi-point flux approximation finite volume schemes for the porous media pressure equation on structured and unstructured grids, Ph.D. thesis, University of Swansea, UK (2007).

[41] Y. Saad, M. H. Schultz, Gmres: A generalized minimal residual algorithm for solving nonsymmetric linear systems, SIAM J. Sci. Stat. Comput. 7 (3) (1986) 856–869.

[42] K. Stüben, Solving reservoir simulation equations, in: 9th International Forum on Reservoir Simulation, Abu Dhabi, United Arab Emirates, 2007.

[43] S. Balay, M. F. Adams, J. Brown, P. Brune, K. Buschelman, V. Eijkhout, W. D. Gropp, D. Kaushik, M. G. Knepley, L. C. McInnes, K. Rupp, B. F. Smith, H. Zhang, PETSc Web page, http://www.mcs.anl.gov/petsc (2014).

[44] J. R. Shewchuk, Triangle: Engineering a 2D Quality Mesh Generator and Delaunay Triangulator, in: Applied Computational Geometry: Towards Geometric Engineering, Vol. 1148 of Lecture Notes in Computer Science, Springer-Verlag, 1996, pp. 203–222.

[45] H. Si, A quality tetrahedral mesh generator and three-dimensional Delaunay triangulator, WIAS technical report No. 13, `http://www.tetgen.org/` (2013).